Computers and Geotechnics 182 (2025) 107133

Contents lists available at ScienceDirect

Computers and Geotechnics

journal homepage: www.elsevier.com/locate/compgeo

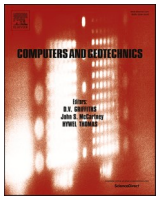

Research Paper

Seismic bearing capacity of rectangular foundations near slopes using the upper bound method

Sheng Xu [a], Xiao-Li Yang [c], Zhen-Yu Yin [a,b,*]

[a] Department of Civil and Environmental Engineering, The Hong Kong Polytechnic University, Hung Hom Kowloon Hong Kong China
[b] Research Centre for Nature-based Urban Infrastructure Solutions, The Hong Kong Polytechnic University, Hong Kong, China
[c] School of Civil Engineering, Central South University, Hunan 410075, China

ARTICLE INFO

Keywords:
Upper bound solution
Seismic bearing capacity
3D failure mechanism
Rectangular foundation
Shape factor

ABSTRACT

When the upper load of a rectangular foundation exceeds its ultimate bearing capacity, its failure mechanism is typically an irregular three-dimensional (3D) geometry. By constructing this 3D failure mechanism, this article introduces a theoretical framework for evaluating the seismic bearing capacity of rectangular foundations adjacent to slopes. This 3D mechanism's profile is the classical multi-block mechanism, and the construction of the end faces follows strict associated flow rule. Additionally, the pseudo-static method is utilized to calculate the action of seismic loads. Finally, an energy balance equation is constructed, from which the upper bound solution for seismic bearing capacity is derived. To facilitate practical design, a simple superposition method is provided to calculate the seismic bearing capacity. The effects of aspect ratio, slope inclination, and distance to the slope edge on the seismic bearing capacity are extensively explored. A shape factor is introduced to investigate the differences in bearing capacity between rectangular and strip foundations, with results indicating that a smaller aspect ratio yields a larger shape factor. The investigation into critical 3D failure mechanisms indicates that an increase in seismic intensity reduces the overall size of the mechanism, while an increase in internal friction angle enlarges it.

1. Introduction

The rectangular foundations' bearing capacity directly impacts the stability and safety of structures, making it a prominent focus in soil mechanics research. With the rapid development of computer technology, many scholars use finite element method (FEM) to calculate the bearing capacity of rectangular foundation (Chwała, 2019; Gourvenec, 2007; Kawa et al., 2016; Mansouri et al., 2019). FEM can accurately simulate complex boundary conditions and heterogeneous material properties, thus improving the accuracy of analysis. On that basis, Sloan (1989) and Krabbenhoft et al. (2005) combined finite element method with limit analysis method to propose finite element limit analysis (FELA). FELA is suitable for analyzing the bearing capacity of foundation without assuming the failure sliding surface. Yang et al. (2003) used the FELA to analyze the lower bound solution of bearing capacity of smooth rectangular foundations along with the associated stress distributions. Many scholars also use FELA to obtain the upper bound solution of rectangular foundations' bearing capacity (Antao et al., 2012; Li et al., 2021; Mohapatra and Kumar, 2019). Mohapatra and Kumar (2019) innovatively used the radial point interpolation method to analyze the impact of different parameters on the bearing capacity and shape factor; Li et al. (2021) expanded the study to clays with linearly increasing undrained strength, proposing a vertical bearing capacity design equation for rectangular foundations considering this effect. Within the framework of FELA, Salgado et al. (2004) and Lyamin et al. (2007) investigated the bearing capacity of rectangular foundations in clay and sand, respectively.

Although FEM and FELA can provide high-precision numerical solutions of rectangular foundation's bearing capacity under complex conditions, they both require large computational resources and time. The analytical solution derived by mathematical or physical formulas can intuitively give the calculation expression of bearing capacity, which is applicable to all possible input parameters. Therefore, many scholars focus on the analytical solution of rectangular foundations' bearing capacity. The limit equilibrium method, widely recognized as a standard analytical technique, has been a subject of debate within geotechnical engineering circles due to concerns regarding its precision (Castelli and Motta, 2010; Izadi et al., 2022). The limit analysis (LA)

* Corresponding author.
E-mail addresses: sheng1211.xu@connect.polyu.hk (S. Xu), yangky@aliyun.com (X.-L. Yang), zhenyu.yin@polyu.edu.hk (Z.-Y. Yin).

https://doi.org/10.1016/j.compgeo.2025.107133
Received 15 August 2024; Received in revised form 8 January 2025; Accepted 5 February 2025
Available online 21 February 2025

method, based on the plastic mechanics theory, can obtain the ultimate load in various complicated cases, and thus is favored by many scholars (Maghferati et al., 2023; Tavakoli et al., 2023). LA method can be divided into the upper bound method and the lower bound method, with the upper bound method requiring the construction of a kinematically admissible velocity field (Michalowski, 2001; Osman, 2019). To construct 3D failure mechanism with kinematically admissible velocity field for rectangular foundations on flat ground, Michalowski (2001) proposed a complex mechanism with a series of conjugate conical blocks, whereas Osman (2019) introduced a mechanism composed of tapered truncated rigid blocks.

The failure mechanism for rectangular foundation near a slopes is markedly different from that for rectangular foundation on flat ground (Cao et al., 2016; De Buhan and Garnier, 1998; Ganjian et al., 2009; Michalowski, 1989; Wang and Yang, 2005). In the beginning, Michalowski (1989) proposed a 3Dfailure mechanism, which consists of multiple triangles and quadrilaterals forming a multi-block mechanism in the vertical slope direction. Subsequently, De Buhan and Garnier (1998) introduced two new failure mechanisms, namely the unstable failure mechanism and the punching failure mechanism. It is noted that the punching failure mechanism extends the classical Prandtl failure mechanism to 3D space. By improving the punching failure mechanism, Wang and Yang (2005) proposed a symmetrical translational mechanism composed of five distinct wedges. Later, following the non-associated flow rule, Ganjian et al. (2009) constructed a rotational failure mechanism with multiple lateral surfaces. To simplify the construction of the failure mechanism, Cao et al. (2016) assumed that both end surfaces are parallel to the vertical plane.

For foundations located near slopes, especially in regions prone to frequent earthquakes, their seismic bearing capacity must be thoroughly considered. Although some scholars prefer to use more complex pseudo-dynamic methods to analyze the structural response under earthquake action (Izadi et al., 2021a,b; Safardoost Siahmazgi et al., 2022; Soufi et al., 2021), the pseudo-static method, which is based on static analysis and considers the inertial forces of the soil, remains the mainstream method for assessing the foundations' seismic bearing capacity(Askari and Farzaneh, 2003; Izadi et al., 2021a,b, Kalourazi et al., 2019, Kumar and Ghosh, 2006, Yamamoto, 2010). This method is widely favored because it strikes an effective balance between computational efficiency and precision. Askari and Farzaneh (2003), Kumar and Ghosh (2006) and Yamamoto (2010) all adopted the upper bound method. The difference is that, the failure mechanisms utilized by Kumar and Ghosh (2006) and Yamamoto (2010)include triangular wedges, logarithmic spiral shear bands, and quadrilateral blocks, while Askari and Farzaneh (2003) employed a multi-block failure mechanism consisting entirely of triangular blocks. Izadi et al. (2021a,b) and Kalourazi et al. (2019) both employed FELA to calculate the lower bound solution for seismic bearing capacity. However, these studies have all focused-on strip footings, and currently, no scholars have investigated the seismic bearing capacity of rectangular foundations adjacent to slopes.

This paper aims to investigate the seismic bearing capacity of rectangular foundations adjacent to slopes using the pseudo-static method and upper bound method. Following the associated flow rule, a 3D multi-block failure mechanism has been established based on the research of Michalowski (1989). The coordinates of each vertex of this 3D failure mechanism can be obtained using the spatial analytic geometry method. Then, by determining a kinematically admissible velocity field, the power generated by all external forces, including seismic inertial forces, and the internal energy dissipation caused by all velocity discontinuity surfaces are calculated. Utilizing the principle of virtual power, an energy balance equation is constructed, from which analytical formulas for the seismic bearing capacity q_u are derived. A superposition method is provided to calculate q_u by adding the contributions of soil weight, cohesion, and overburden load to the bearing capacity.

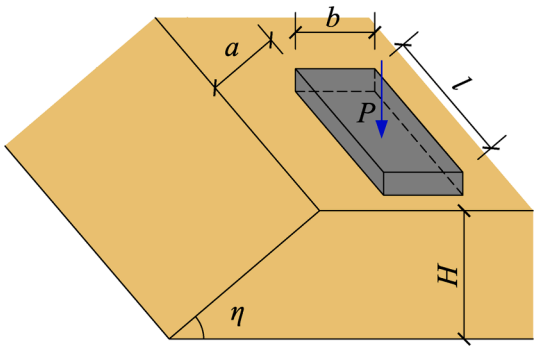

Fig. 1. Schematic diagram of a rectangular foundation near a slope.

2. Problem description

2.1. Objective

In the process of urban planning, to enhance land use efficiency, obtain better landscape views, and for other considerations, many rectangular foundations have to be located near slopes. Facing the challenge in seismic bearing capacity assessment posed by this layout, it is essential to first construct a corresponding analysis model. As shown in Fig. 1, a rigid rectangular foundation is placed on a slope with an inclination angle of η. The length and width of this rectangular foundation are l and b, respectively, and its horizontal distance from the edge of the slope is a. H represents the vertical height of the slope. It is assumed that in the initial failure stage, the vertical load that the rectangular foundation can withstand is P. Dividing this load by the area of the foundation yields the value of the seismic bearing capacity q_u. According to the classic Terzaghi bearing capacity equation, q_u can be expressed as the sum of the contributions to the bearing capacity from the soil cohesion c, overburden load q, and the unit weight of the soil γ, with the specific formula as follows:

$$q_u = \frac{P}{lb} = cN_{cE} + qN_{qE} + 0.5\gamma bN_{\gamma E} \tag{1}$$

where N_{cE}, N_{qE} and $N_{\gamma E}$ denote the seismic bearing capacity factors associated with c, q, γ, respectively.

2.2. Assumptions

(1) The soil under rectangular foundation is isotropic and homogeneous, which conforms to Mohr-Coulomb criteria.
(2) The rectangular foundation is a shallow rigid foundation with little deformation and the foundation-soil interface is rough.
(3) The slope is high enough that the failure mechanism only occurs above the slope toe.

3. Upper bound solution for 3D seismic bearing capacity

3.1. Kinematic method

After establishing the analytical model, it is necessary to determine the failure mechanism and construct a velocity field that satisfies the geometric equations and velocity boundary conditions (Hou and Yang, 2022; Li et al., 2020; Xu et al., 2023; Zhang and Yang, 2023; Zhong and Yang, 2022). Then, the energy dissipation in the velocity field is calculated, and the upper bound solution can be obtained by solving the energy balance equation. This energy balance equation can be expressed as:

$$\int_A T_i v_i dA + \int_V F_i v_i dV = \int_V \sigma_{ij}\varepsilon_{ij} dV \tag{2}$$

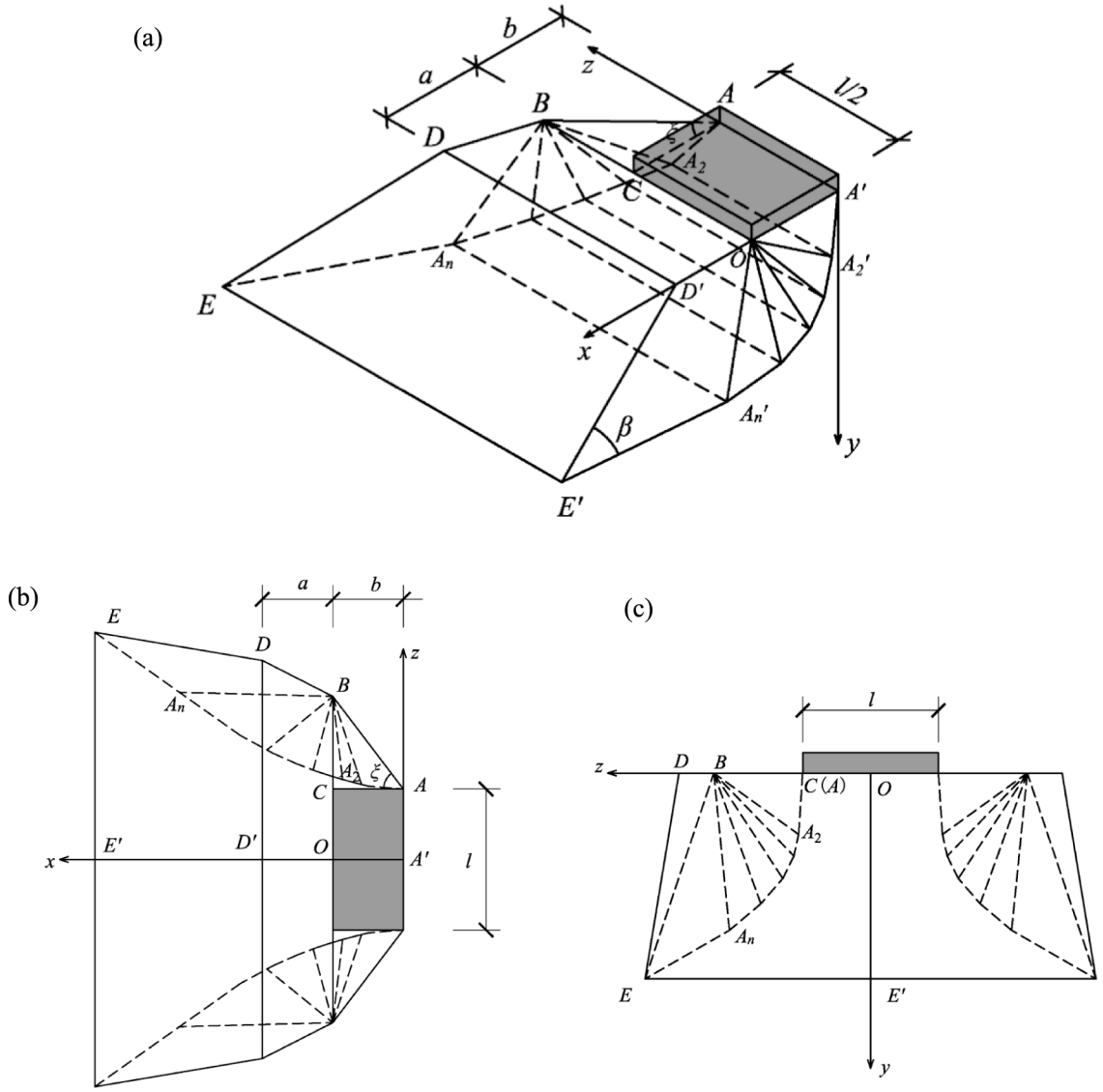

Fig. 2. 3D collapse mechanism of a rectangular foundation from Michalowski (1989): (a) 3D view (b) top view (c) side view.

where v_i and ε_{ij} represent the velocity field and the strain field, respectively, σ_{ij} represent the stress field, T_i and F_i represent the surface load and body load, respectively. A and V represent the area and volume of the failure region, respectively.

3.2. 3D failure mechanism

The geometric complexity of the 3D mechanism makes analytical calculations quite challenging. Under static conditions, when a rectangular foundation near a slope fails, the soil beneath it extends a considerable distance towards both ends, as demonstrated by the failure mechanism presented by Wang and Yang (2005). Because the restraint of the slope on the soil beneath the foundation is clearly weaker than the restraint of the soil on both sides, under the action of seismic forces, more soil beneath the foundation slides towards the slope, while the extension towards the ends is reduced. Specifically, as shown in Fig. 2, this 3D mechanism consists of multiple rigid moving blocks separated by planar velocity discontinuity surfaces. All blocks are prisms with bases that are either triangular or quadrilateral.

This failure mechanism develops from point A towards one side with an angle of ξ. In other words, ξ represents the angle between line segments AB and AC. The most critical step involves constructing the end surface $BAA_2A_3\cdots A_nED$, which is achieved through point-to-point iteration. Note that this end surface $BAA_2A_3\cdots A_nED$ is not a single plane; rather, it comprises n-1 spatial triangular failure surfaces and one quadrilateral failure surface, all of which are not coplanar. Each failure

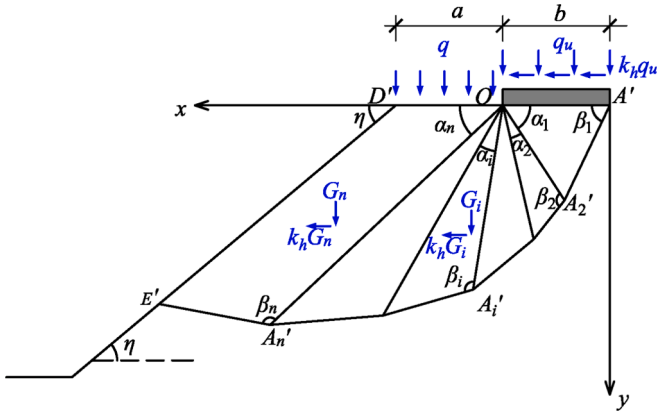

Fig. 3. Section view of the 3D mechanism along *xoy* plane.

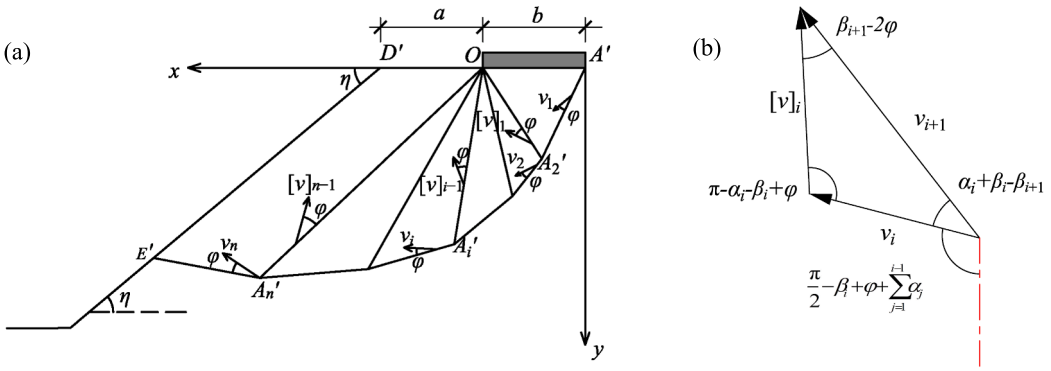

Fig. 4. (a) Velocity field and (b) velocity hodograph of the failure mechanism (section along *xoy* plane).

surface adheres to the associated flow rule, with the specific calculation method detailed in the Appendix A. The cross-section of this three-dimensional failure mechanism along the *xoy* plane is shown in Fig. 3. It can be seen that this cross-section is essentially a multi-block failure mechanism, which was used by some scholars to evaluate the bearing capacity of strip footings placed on slopes (Askari and Farzaneh, 2003; Yang, 2009). The angles α_i and β_i ($i = 1, 2. 3, \ldots, n$) of each block in the cross-section are as yet unspecified.

3.3. Velocity field and power calculation

Fig. 4(a) presents the velocity field of this 3D collapse mechanism in cross-section form, along with the velocity vector triangle of the *i*-th block. $v_i (1 \leqslant i \leqslant n)$ and $[v]_i (1 \leqslant i \leqslant n-1)$ respectively represent the velocities of the block's base and the common surface with the adjacent block. As shown in Fig. 4(b), the sine rule is used to derive the expressions for v_i and $[v]_i$ as follows:

$$v_i = \prod_{j=1}^{i-1} \frac{\sin(\alpha_j + \beta_j - 2\varphi)}{\sin(\beta_{j+1} - 2\varphi)} v_1 \, 1 \leqslant i \leqslant n \tag{3}$$

$$[v]_i = \frac{\sin(\alpha_i + \beta_i - \beta_{i+1})}{\sin(\beta_{i+1} - 2\varphi)} \prod_{j=1}^{i-1} \frac{\sin(\alpha_j + \beta_j - 2\varphi)}{\sin(\beta_{j+1} - 2\varphi)} v_1 \, 1 \leqslant i \leqslant n-1 \tag{4}$$

As shown in Fig. 4(b), the velocity of the *i*-th block makes an angle $\frac{\pi}{2} - \beta_i + \sum_{j=1}^{i-1} \alpha_j + \varphi$ with the vertical direction. Therefore, the vertical component v_{iy} and the horizontal component v_{ih} of the velocity of the *i*-th block are given by:

$$v_{iy} = v_i \sin(\beta_i - \sum_{j=1}^{i-1} \alpha_j - \varphi) \tag{5}$$

$$v_{ih} = v_i \cos(\beta_i - \sum_{j=1}^{i-1} \alpha_j - \varphi) \tag{6}$$

The energy dissipation of each sliding surface is the product of the soil's cohesion, the velocity component along the sliding surface, and the area of the sliding surface. Assuming the areas of the bottom surface, end surface, and shared surface of each block are S_i, S_i' and S_i'', respectively, the total energy dissipation D_{int} of this 3D failure mechanism can be expressed as the sum of the energy dissipation of these sliding surfaces, namely:

$$D_{int} = \sum_{i=1}^{n} c v_i S_i \cos\varphi + \sum_{i=1}^{n} c v_i S_i' \cos\varphi + \sum_{i=2}^{n} c [v]_i S_i'' \cos\varphi \tag{7}$$

Note that the method for calculating S_i, S_i', S_i'' is detailed in Appendix A. The external forces acting on a rectangular foundation consist of three components (the ultimate load q_u, the overburden load q, the soil gravity G_i) and their seismic inertia force. The energy dissipated by these external forces is calculated as follows:

$$W_{q_u} = \frac{q_u l b}{2} (v_{1y} + k_h v_{1h}) \tag{8}$$

$$W_q = q S_a (v_{1y} + k_h v_{1h}) + q S_b (v_{ny} + k_h v_{nh}) \tag{9}$$

$$W_\gamma = \sum_{i=1}^{n} \gamma V_i (v_{iy} + k_h v_{ih}) \tag{10}$$

where W_{q_u}, W_q, W_γ represent the power caused by q_u, q, and G_i respectively; $S_b = \frac{b^2 \tan\xi}{2}$, $S_a = \frac{a}{2}(\frac{l}{2} + b\tan\xi + z_D)$ represent the area of plane *ABC*, plane *OBDD′* respectively; V_i is the volume of the *i*-th block, with its formula detailed in Appendix A; k_h is the horizontal seismic acceleration coefficient By superimposing these powers, the total external power W_{ext} of the failure mechanism can be obtained as:

$$W_{ext} = W_{q_u} + W_q + W_\gamma \tag{11}$$

Setting $W_{\text{ext}} = D_{int}$, by solving this equation, an explicit expression for the seismic bearing capacity q_u can be derived as:

$$q_u = \frac{2(D_{int} - W_q - W_\gamma)}{l b (v_{1y} + k_h v_{1h})} \tag{12}$$

According to Eq. (1), the expressions for seismic bearing capacity factor $N_{\gamma E}$, N_{qE} and N_{cE} can be expressed as:

$$N_{\gamma E} = -\frac{4 W_\gamma}{\gamma l b^2 (v_{1y} + k_h v_{1h})} \tag{13}$$

$$N_{qE} = -\frac{2 W_q}{q l b (v_{1y} + k_h v_{1h})} \tag{14}$$

$$N_{cE} = \frac{2 D_{int}}{c l b (v_{1y} + k_h v_{1h})} \tag{15}$$

From the derivation process, the seismic bearing capacity is only related to $2n + 1$ angular variables, namely:

$$q_u = f(\alpha_i, \beta_i, \xi) \tag{16}$$

Different values of variables will yield different values of q_u, $N_{\gamma E}$, N_{qE} or N_{cE}. According to the limit analysis theorem, the upper bound solution exceeds the true solution. To approximate the true solution more closely, it is necessary to determine the smallest upper bound solution. This paper employs the multi-objective sequential quadratic programming (SQP) algorithm to calculate the minimum upper bound solution. To ensure the rationality of this 3D failure mechanism and the velocity field, certain constraints should be incorporated into the algorithm, as

Table 1
Some constraints to ensure the rationality of the failure mechanism and velocity field.

	Constraints/Conditions
Geometric compatibility	$\sum_{j=1}^{n}\alpha_j = \pi$, $\alpha_i + \beta_i > \beta_{i+1}$ and $0 < \pi + \eta - \alpha_n - \beta_n < \pi$
Kinematic admissibility	$v_{i+1} > v_i$
Range of values	$0 < \alpha_i, \eta < \pi/2$, $0 < \beta_i < \pi$

Table 2
The seismic bearing capacity q_u versus different numbers of blocks n.

n	$\eta = 10°$	$\eta = 20°$	$\eta = 30°$
4	263.57	247.75	225.53
5	261.67	246.47	224.78
6	260.78	245.87	224.44
7	260.29	245.53	224.24
8	259.99	245.35	224.14

Note: $b = 1$ m, $a/b = 1$, $l/b = 2$, $c = 10$ kPa, $\gamma = 20$ kN/m^3, $k_h = 0.1$, $\varphi = 20°$.

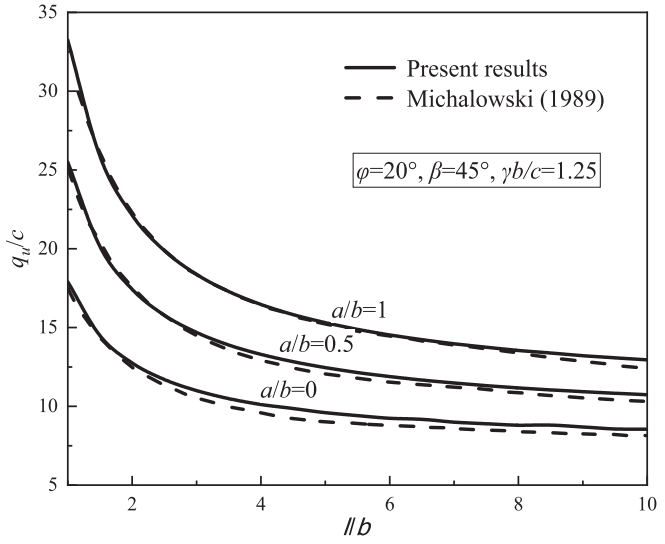

Fig. 5. Comparison of dimensionless bearing capacity q_u/c with l/b and a/b.

presented in Table 1.

3.4. Convergence of solution

The 3D failure mechanism includes n spatial blocks. To obtain the upper bound solution, the volume of each block, the coordinates of the corner points, and the area of each velocity discontinuity surface need to be calculated. To reduce the computational workload, a convergence study was performed to determine the optimal number of rigid blocks for identifying the minimum upper bound solution. From Table 2, it can be seen that, as n increases from 4 to 8, both the seismic bearing capacity value and the range of variation continuously decrease. When the number of blocks is sufficiently large, the seismic bearing capacity will converge to a fixed value. When n increases from 7 to 8, the change in seismic bearing capacity is less than 0.1 %. Therefore, in all subsequent calculations, the number of blocks n is set to 8.

4. Validation

Considering that no previous research has addressed the bearing capacity of rectangular foundations near slopes under seismic conditions, this study's validation is divided into two parts: comparison with available theoretical results and comparison with numerical simulation results. If these two validation parts are successful, the bearing capacity calculation method proposed in this paper will be confirmed as valid.

4.1. Comparison with the available theoretical results

The comparison of this section can also be subdivided into three sections. First, under static conditions, the present results will be compared with the static bearing capacity results for rectangular foundations placed on slopes calculated by Michalowski (1989). This comparison will validate the effectiveness of the 3D failure mechanism. Then, under seismic conditions, the present results will be compared with the bearing capacity results for strip footings near slopes to demonstrate the effective assessment of seismic load effects. Finally, by setting the slope angle to zero and a large aspect ratio, a comparison can be made between the present results and the bearing capacities of strip footings on flat ground as documented in previous research. This would demonstrate that the theoretical framework proposed retains its validity when applied to strip foundations on horizontal terrains.

Fig. 5 compares the static bearing capacity results of the rectangular foundations adjacent to slopes presented in this paper with those of Michalowski (1989), considering different lengths and different distances to the slope edge. Fig. 5 shows that with an increase in l/b value, the value of q_u/c continuously decreases, and the rate of decrease also slows down. As expected, for a given aspect ratio l/b, the farther the foundation is from the slope edge, the greater the bearing capacity. Most importantly, for any given aspect ratio and distance to the slope edge, the maximum difference between the results of this paper and those of Michalowski (1989) does not exceed 3 %. This proves that the 3D failure mechanism provided is effective, and the upper bound solution for the static bearing capacity of the rectangular foundation derived from it is accurate. Note that the discrepancies between the two sets of results are primarily attributed to the distinct optimization algorithms employed: this study utilizes the SQP algorithm, whereas Michalowski (1989) employed an iterative numerical method.

Table 3 compares the seismic bearing capacity results of rectangular foundations obtained in this study with those of strip footings obtained in other studies for $k_h = 0.15$ and 0.30, $\varphi = 30°$ and 45°, $\eta = 15°$ and 30°. It is worth mentioning that Askari and Farzaneh (2003) and Yamamoto (2010) also used the upper bound method of limit analysis. Table 3 shows that for all combinations of seismic acceleration coefficient k_h, internal friction angle φ, and slope inclination η, the bearing capacity results of this paper are the highest. This is because 3D mechanisms are typically able to involve more soil in the bearing process. Meanwhile, in 3D conditions, factors such as lateral constraints and friction of the soil contribute more significantly to the bearing capacity. Moreover, as the value of l/b increases, the bearing capacity results of this paper gradually approach those of the strip footing calculated by Askari and Farzaneh

Table 3
Comparison of dimensionless bearing capacity q_u/c.

k_h	φ (°)	η (°)	Present results ($l/b = 10$)	Present results ($l/b = 50$)	Present results ($l/b = 100$)	Askari and Farzaneh (2003)	Yamamoto (2010)
0.15	30	15	26.18	22.24	21.73	21.46	20.32
	45	30	75.04	57.22	55.51	49.83	46.25
0.30	30	15	16.94	14.75	14.47	14.28	13.23
	45	30	45.32	33.72	32.16	29.07	25.43

Note: $b = 1$ m, $a/b = 0.5$, $\gamma b/c = 1$.

Table 4
Comparison of $N_{\gamma E}$ with previous studies.

φ (°)	This study	Soubra (1999)	Zhu (2000)	Michalowski (1997)	Chen (1975)	Izadi et al. (2021a,b)
15	2.18	2.10	1.94	1.94	2.94	
20	4.76	4.67	4.47	4.47	6.20	
25	10.25	10.06	9.76	9.77	12.96	
30	22.45	21.88	21.38	21.39	27.67	15.06
35	51.36	49.62	48.65	48.68	61.47	
40	126.83	120.96	118.76	118.83	145.19	79.19
45	351.65	328.88	322.62	322.84	374.02	

Note: $k_h = 0.0$, $\beta = 0$, $b = 1$ m, $a = 0$, $l/b = 100$.

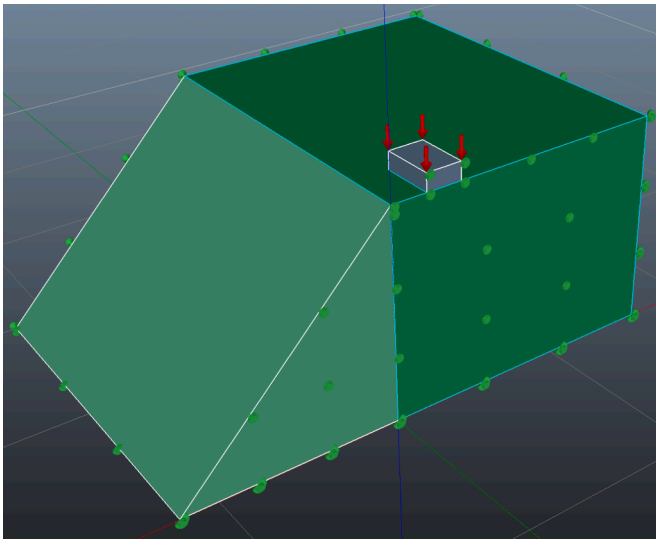

Fig. 6. Model of a rectangular foundation near a slope in OPTUM G3.

(2003), which again demonstrates the accuracy of the upper bound solution in this paper. Additionally, the results of Askari and Farzaneh (2003) are consistently higher than those of Yamamoto (2010), which is due to Askari and Farzaneh (2003) using a logarithmic spiral failure mechanism while Yamamoto (2010) used a multi-block failure mechanism.

With inclination angle β set to 0 and the aspect ratio l/b set to 100, the slope-adjacent rectangular foundation discussed in this paper effectively becomes a strip footing on flat ground. Table 4 illustrates a comparison between the results from this research and those from prior research on strip footings. Among them, Soubra (1999), Zhu (2000), Michalowski (1997), and Chen (1975), like this paper, all employed the upper bound method. For all internal friction angles, the present results are larger than those of Soubra (1999), Zhu (2000), and Michalowski (1997), which proves that the traditional plane strain analysis for strip footing bearing capacity calculations results in a conservative estimate. Chen (1975) used the classic Prandtl mechanism, hence its results are the largest. In contrast, Izadi et al. (2021a,b) used utilized the finite element limit analysis lower bound method, resulting in the smallest values.

4.2. Comparison with the numerical simulation results

A model of a rectangular foundation adjacent to a slope is constructed using OPTUM G3, a 3D geotechnical analysis software, as shown in Fig. 6. OPTUM G3 provides a combination of limit analysis and finite element method, and supports automatic mesh refinement, which significantly improves efficiency while ensuring calculation accuracy. To establish the model, the corresponding slope geometric model is first created, noting that the length of the slope needs to be much greater than the length of the foundation. The slope soil is set to follow the Mohr-Coulomb criterion, and the foundation is set as a rigid material. Then, standard boundary conditions are set. The most critical step is to add loads: according to the pseudo-static method, a fixed horizontal acceleration is added to the slope soil and foundation to simulate seismic loads. Additionally, a multiplier distributed load is added to the rectangular foundation. Finally, the number of elements is set to 2000, and the number of adaptive iterations is set to 3. The element type is chosen as the upper bound. After running this model in OPTUM G3, the upper bound solution of the seismic bearing capacity can be obtained. The numerical solutions and the analytical solutions under different conditions are recorded in Table 5.

From Table 5, the numerical results calculated by OPTUM G3 are very close to the analytical results obtained from the theoretical framework of this paper, with an average difference of no more than 5 %. This strongly demonstrates the effectiveness and accuracy of present results. However, since the analytical method in this study provides a clear formula for computing the seismic bearing capacity without the need for separate modeling for different scenarios, it has a broader practical significance. Assuming $k_h = 0.1$, $\eta = 45°$, $a/b = 1$, $l/b = 3$, $\gamma = 18$ kN/m^3, $c = 10$ kPa, Fig. 7 shows the displacement cloud diagrams of the slope-adjacent rectangular foundation at failure for four different internal friction angles. From Fig. 7, as the internal friction angle increases, the geometric dimensions of failure mechanism are also continuously increasing. Moreover, the failure mechanism shown in Fig. 7 is very similar to that presented in this paper (Fig. 2), which further proves the accuracy of the methods used in this paper.

5. Results and discussions

5.1. Superposition method

This paper provides two methods to calculate the seismic bearing capacity q_u of rectangular foundations near slopes. Method 1 is a superposition method, where the contributions of c, q, and γ to q_u are superimposed to obtain q_u. Its detailed procedure is to calculate $N_{\gamma E}$, N_{qE} and N_{cE} according to Eqs. (13)–(15) and then substitute them into Eq. (1). This superposition method does not consider soil weight when calculating N_{qE} and N_{cE}, and does not consider cohesion and overburden load when calculating $N_{\gamma E}$. Therefore, the superposition method actually considers two different failure mechanisms, making it conservatively safe when applied in practical engineering. Method 2 is a joint method, which applies the Eq. (12) to compute seismic bearing capacity directly.

Table 5
Comparisons of bearing capacity q_u from present analytical formulas with those from numerical simulation.

φ (°)	$l/b = 2$		$l/b = 5$		$l/b = 10$	
	Present results (kPa)	Numerical results (kPa)	Present results (kPa)	Numerical results (kPa)	Present results (kPa)	Numerical results (kPa)
20	182.34	182.94	127.26	117.93	108.09	105.00
25	262.45	266.95	178.58	178.09	149.66	140.66
30	394.18	405.83	260.83	283.21	215.11	236.74
35	626.11	648.69	401.59	444.98	355.17	365.00
40	1046.98	1119.86	731.24	791.44	611.27	643.47

Note: $k_h = 0.1$, $\eta = 45°$, $a/b = 1$, $\gamma = 18$ kN/m^3, $c = 10$ kPa.

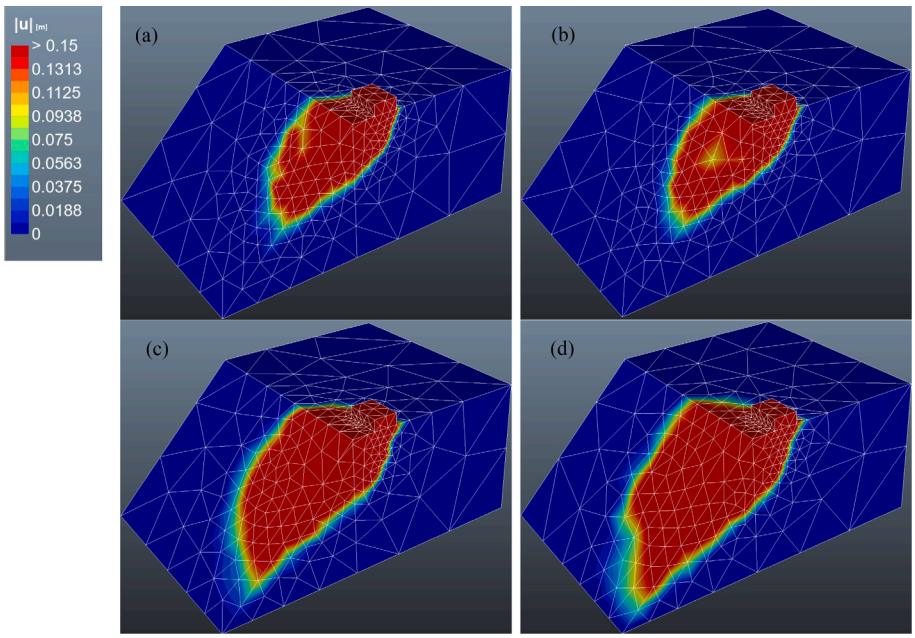

Fig. 7. Displacement contours of rectangular foundation near a slope at failure for (a) $\varphi' = 20°$, (b) $\varphi' = 25°$, (c) $\varphi' = 30°$, (d) $\varphi' = 35°$.

Table 6
Comparison of seismic bearing capacity q_u using two methods.

φ (°)	$l/b = 1$ Method 1 q_{super}(kPa)	Method 2 q_u(kPa)	Difference (%)	$l/b = 2$ Method 1 q_{super}(kPa)	Method 2 q_u(kPa)	Difference (%)	$l/b = 5$ Method 1 q_{super}(kPa)	Method 2 q_u(kPa)	Difference (%)
25	539.74	565.61	4.57	364.82	385.18	5.28	256.59	273.03	6.02
30	929.71	970.64	4.22	608.01	637.07	4.56	409.93	432.18	5.15
35	1708.56	1777.30	3.87	1082.21	1126.37	3.92	698.34	730.76	4.44
40	3420.42	3544.72	3.51	2100.01	2178.31	3.59	1295.63	1346.86	3.80
45	7713.38	7977.71	3.31	4591.74	4736.21	3.05	2700.38	2788.48	3.16

Note: $k_h = 0.1$, $a/b = 1$, $\eta = 20°$, $c = 10$ kPa, $\gamma = 20$ kN/m^3.

Table 7
Seismic bearing capacity factor $N_{\gamma E}$ of rectangular footings ($a/b = 1$).

		$\eta = 10°$						$\eta = 20°$					
		l/b											
k_h	φ (°)	1	1.5	2	3	5	10	1	1.5	2	3	5	10
0.0	15	4.46	3.60	3.27	3.11	2.63	2.33	3.46	2.86	2.55	2.24	1.98	1.78
	20	9.07	7.62	6.88	6.13	5.52	5.05	8.54	6.94	6.13	5.31	4.64	4.13
	25	21.52	17.52	15.49	13.45	11.79	10.52	19.01	15.22	13.31	11.36	9.77	8.54
	30	51.36	40.67	35.28	29.86	25.46	22.11	42.32	33.15	28.54	23.89	20.11	17.22
	35	128.55	99.23	84.50	69.67	57.67	48.54	97.95	75.15	63.83	52.17	42.79	35.60
	40	351.10	264.48	221.00	177.29	142.00	115.13	243.73	183.05	152.60	121.97	97.24	78.41
	45	1096.43	805.50	660.37	514.62	397.12	307.77	677.00	497.96	408.19	408.19	318.05	245.39
0.1	15	1.72	1.49	1.37	1.29	1.22	1.11	1.14	0.91	0.78	0.65	0.53	0.43
	20	5.64	4.58	3.67	3.32	3.04	2.82	3.97	3.24	2.87	2.49	2.18	1.93
	25	12.18	10.03	8.95	7.84	6.94	6.25	10.18	8.16	7.15	6.12	5.29	4.66
	30	29.87	23.90	20.89	17.86	15.40	13.52	24.06	18.94	16.36	13.76	11.66	10.05
	35	75.00	58.48	50.17	41.81	35.04	29.88	56.61	43.68	37.20	30.68	25.39	21.37
	40	201.92	153.58	129.30	104.88	85.16	70.14	139.53	105.59	88.55	71.40	57.56	47.04
	45	610.72	453.35	374.40	295.11	231.15	182.50	377.86	280.10	231.08	181.90	142.28	112.22
0.2	20	1.95	1.74	1.55	1.37	1.22	1.10	1.23	0.97	0.84	0.70	0.57	0.46
	25	5.94	4.99	4.49	3.98	3.56	3.23	4.46	3.60	3.16	2.72	2.36	2.08
	30	15.76	12.77	11.26	9.73	8.48	7.53	11.97	9.51	8.27	7.02	6.00	5.23
	35	40.74	32.13	27.80	23.43	19.90	17.20	29.86	23.26	19.94	16.61	13.91	11.86
	40	109.89	84.49	71.73	58.89	48.51	40.60	75.07	57.32	48.41	39.46	32.24	26.75
	45	325.91	244.40	203.51	162.40	129.23	103.99	201.69	150.92	125.46	125.46	99.89	79.30

Table 8
Seismic bearing capacity factor N_{cE} of rectangular footings ($a/b = 1$).

		$\eta = 10°$						$\eta = 20°$					
		l/b											
k_h	φ (°)	1	1.5	2	3	5	10	1	1.5	2	3	5	10
0.0	15	24.73	20.19	17.87	15.49	13.52	11.97	23.99	19.44	17.12	14.74	12.77	11.23
	20	38.21	30.36	26.39	22.33	18.99	16.38	35.98	28.42	24.59	20.68	17.47	14.97
	25	61.26	47.53	40.57	33.52	27.73	23.23	55.56	42.90	36.49	30.00	24.69	20.57
	30	103.39	78.37	65.75	53.00	42.58	34.51	89.62	67.60	56.63	45.45	36.39	29.38
	35	186.34	138.23	114.88	89.73	69.85	54.46	152.33	112.63	92.85	72.88	56.66	44.18
	40	367.01	266.96	216.46	165.78	124.69	93.11	278.41	202.33	164.25	125.92	94.92	71.13
	45	811.79	578.91	462.18	344.91	250.16	177.62	562.57	402.07	321.59	240.79	175.56	125.69
0.1	15	19.80	16.43	14.70	12.92	11.44	10.27	19.50	16.06	14.28	12.46	10.93	9.74
	20	30.10	24.29	21.32	18.29	15.78	13.82	28.82	23.08	20.16	17.17	14.70	12.77
	25	47.41	37.28	32.12	26.89	22.59	19.23	43.79	34.20	29.33	24.41	20.37	17.23
	30	78.26	60.02	50.81	41.50	33.86	27.94	68.91	52.66	44.44	36.12	29.34	24.08
	35	137.80	102.99	85.73	68.28	53.95	42.93	114.24	85.43	71.02	56.32	44.44	35.28
	40	262.25	192.85	157.01	121.74	93.09	71.04	202.51	148.74	121.45	94.18	72.01	55.03
	45	556.29	399.95	321.52	242.68	178.92	130.01	393.48	283.33	228.10	172.60	127.76	93.44
0.2	15	15.46	12.95	11.73	10.48	9.43	8.59	15.30	12.87	11.60	10.27	9.16	8.27
	20	22.90	18.83	16.74	14.59	12.80	11.40	22.40	18.25	16.13	13.94	12.12	10.69
	25	35.54	28.40	24.76	21.05	17.99	15.59	33.54	26.59	23.05	19.47	16.48	14.17
	30	57.61	44.78	38.32	31.76	26.39	22.19	51.87	40.12	34.19	28.18	23.23	19.41
	35	98.70	74.95	62.94	50.79	40.90	33.24	84.12	63.53	53.19	42.77	34.29	27.76
	40	182.46	135.56	111.63	88.05	68.29	53.31	144.75	107.69	88.24	69.28	53.81	41.98
	45	373.66	270.80	219.42	167.76	125.93	93.79	270.32	196.36	160.35	121.93	91.75	68.62

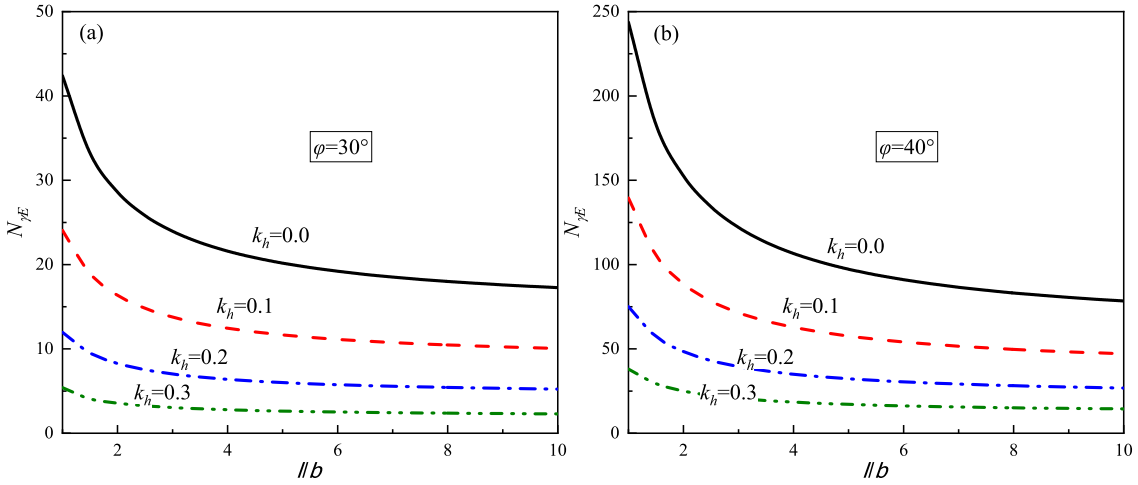

Fig. 8. The variation of $N_{\gamma E}$ versus l/b for (a) $\varphi = 30°$and (b) $\varphi = 40°$ ($a/b = 1$, $\eta = 20°$).

Table 6 compares the seismic bearing capacity obtained using these two methods for different values of l/b and φ. As expected, Method 1, the superposition method, usually provides a more conservative upper bound solution for q_u. However, the maximum difference between the two methods is only 6.02 %, which is within the permissible error range for practical engineering. Compared to the complex optimization process of Method 2, the superposition method only requires checking design tables based on the actual conditions to obtain the corresponding values of $N_{\gamma E}$, N_{cE} and N_{qE}, and then calculating the seismic bearing capacity using Eq. (1). Tables 7 and 8 respectively present the $N_{\gamma E}$ and N_{cE} values for rectangular foundations with different aspect ratios (l/b) under various conditions, which can be used as design tables. Therefore, the superposition method is highly recommended for the practical design of rectangular foundations.

5.2. Parametric analysis

In the subsequent analysis, it is assumed that the rectangular foundation's width is 1 m ($b = 1$ m), and there is no overburden pressure ($q = 0$). Compared to numerical simulation methods, one major advantage of analytical methods is that their solutions are derived from mathematical or physical formulas, making it very convenient to analyze the impact of various parameters. According to the analytical formula for q_u, the factors influencing the value of q_u mainly include seismic acceleration coefficients k_h, aspect ratio l/b, slope inclination angle η, and the distance to the edge of the slope a.

5.2.1. Effect of the aspect ratio

Assuming $a/b = 1$, $\eta = 20°$, Figs. 8 and 9 respectively depict the variation of $N_{\gamma E}$ and N_{cE} with aspect ratio l/b, considering four sets of different seismic acceleration coefficients ($k_h = 0.0$, 0.1, 0.2, 0.3) and two sets of different internal friction angles ($\varphi = 30°$ and 40°). As

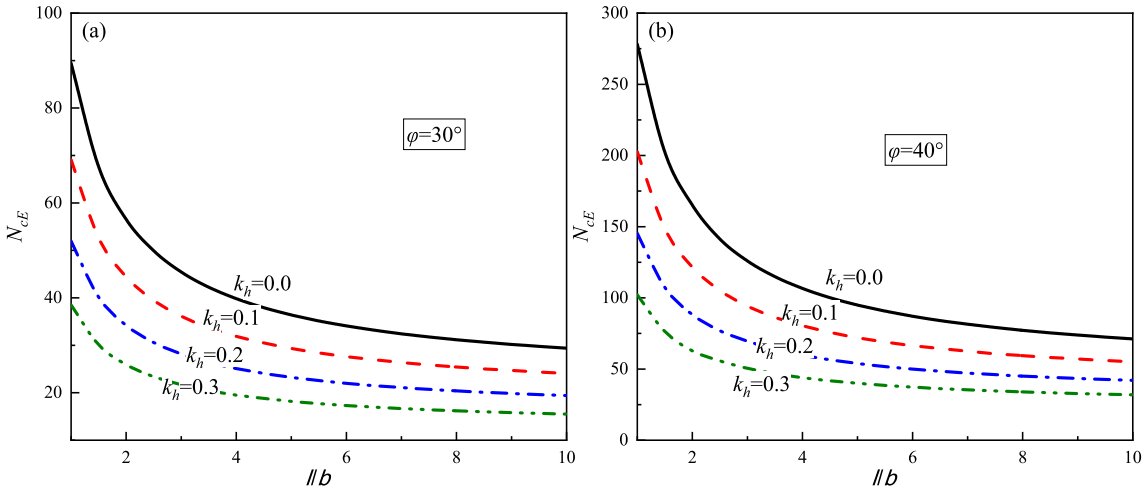

Fig. 9. The variation of N_{cE} versus l/b for (a) $\varphi = 30°$and (b) $\varphi = 40°$ ($a/b = 1$, $\eta = 20°$).

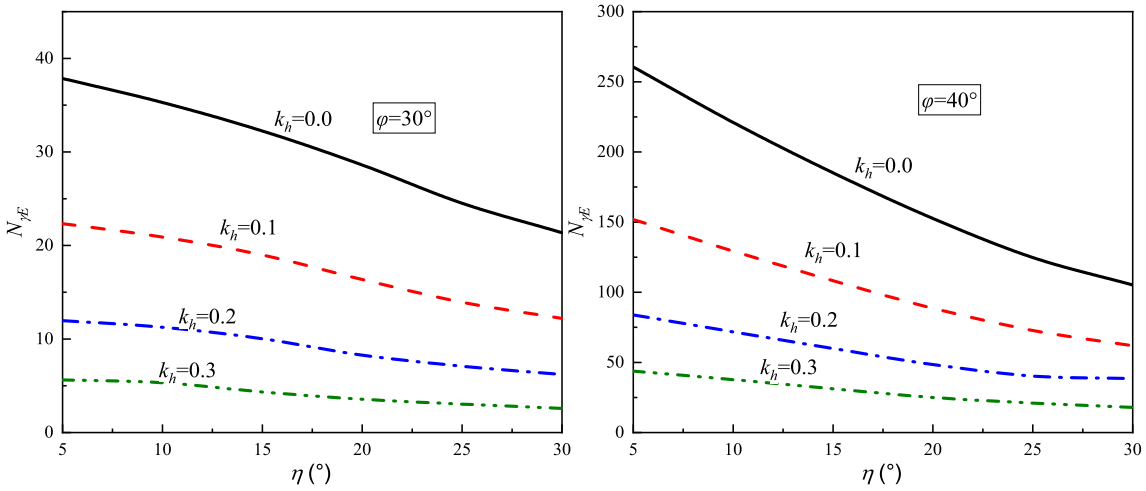

Fig. 10. The variation of $N_{\gamma E}$ versus η for (a) $\varphi = 30°$and (b) $\varphi = 40°$ ($a/b = 1$, $l/b = 2$).

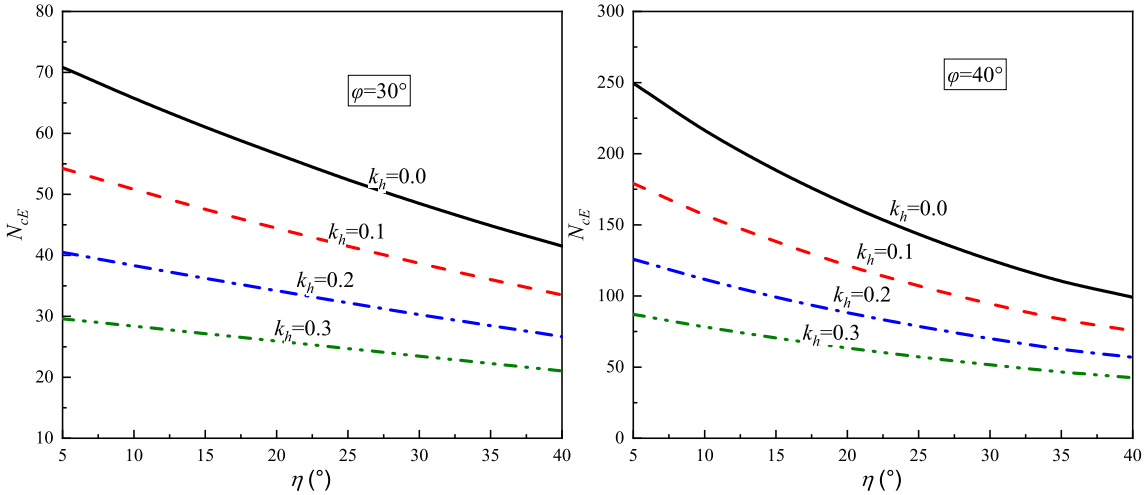

Fig. 11. The variation of N_{cE} versus η for (a) $\varphi = 30°$and (b) $\varphi = 40°$ ($a/b = 1$, $l/b = 2$).

expected, with an increase in k_h, both $N_{\gamma E}$ and N_{cE} values continuously decrease. Moreover, the influence of k_h on $N_{\gamma E}$ is more significant than on N_{cE}. For instance, when $\varphi = 30°$ and $l/b = 1$, as k_h increases from 0.0 to 0.3, $N_{\gamma E}$ decreases by 87.2 %, while N_{cE} only decreases by 57.0 %. As the aspect ratio l/b increases, both $N_{\gamma E}$ and N_{cE} values gradually decrease, but the rate of decrease continuously slows down. For example, when $\varphi = 30°$ and $k_h = 0$, as l/b increases from 1 to 4, $N_{\gamma E}$ decreases by 21.6, whereas it only decreases by 4.3 when l/b increases

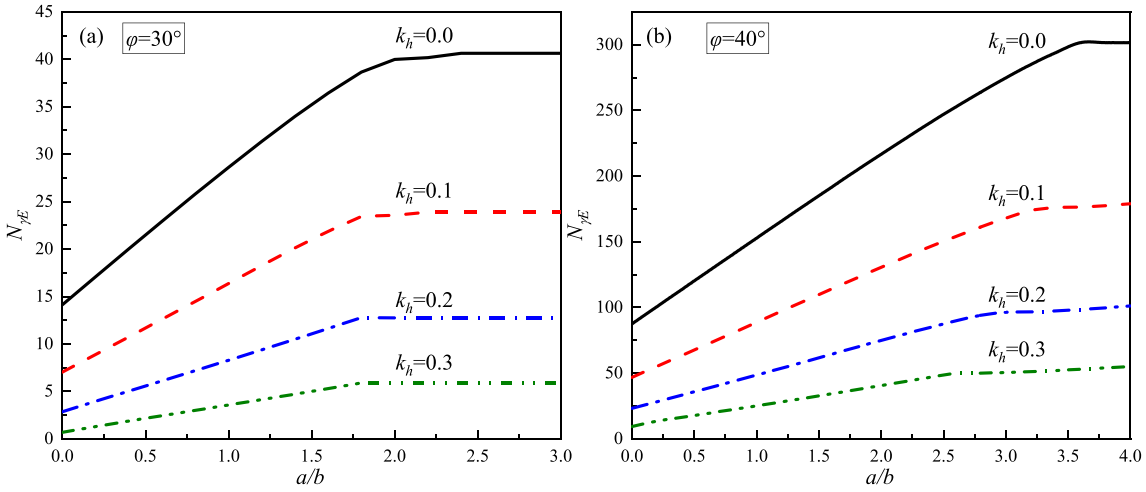

Fig. 12. The variation of $N_{\gamma E}$ versus a/b for (a) $\varphi = 30°$and (b) $\varphi = 40°$ ($\eta = 20°$, $l/b = 2$).

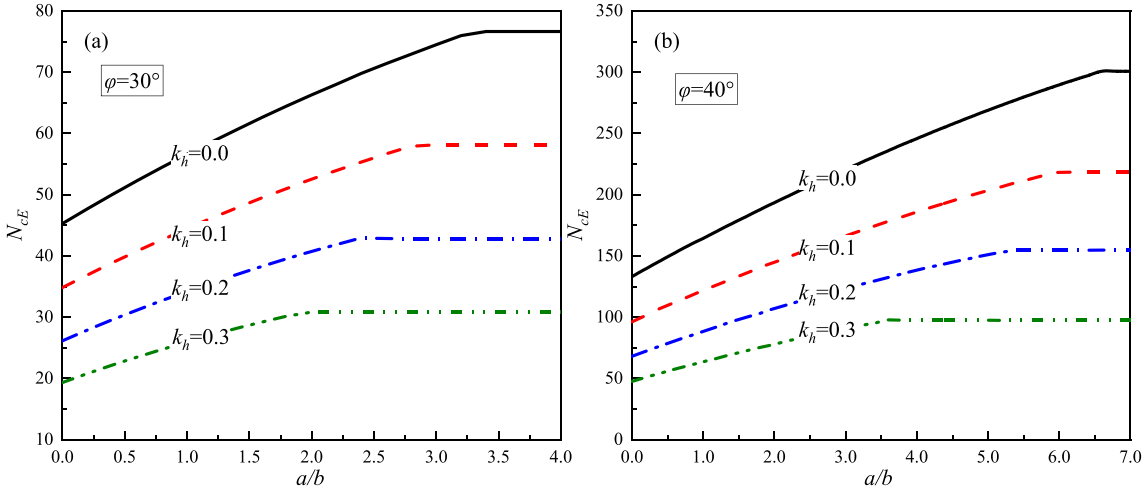

Fig. 13. The variation of N_{cE} versus a/b for (a) $\varphi = 30°$and (b) $\varphi = 40°$ ($\eta = 20°$, $l/b = 2$).

from 4 to 10. Eventually, the bearing capacity factors converge to a fixed value, which is very close to the seismic bearing capacity factor values of strip footings.

5.2.2. *Effect of the slope inclination*

Assuming $a/b = 1$, $l/b = 2$, Figs. 10 and 11 respectively show the variation of the seismic bearing capacity factors ($N_{\gamma E}$ and N_{cE}) with slope inclination η, considering $k_h = 0.0$, 0.1, 0.2, 0.3 and $\varphi = 30°$, 40°. From Fig. 10, as the slope inclination η increases, the value of $N_{\gamma E}$ almost decreases linearly. Additionally, for different values of k_h, the increase in η leads to almost the same rate of decrease in $N_{\gamma E}$. Specifically, when η increases from 5° to 30° and $\varphi = 40°$, with k_h values of 0.0, 0.1, 0.2, $N_{\gamma E}$ decreases by 59.6 %, 59.3 %, 59.2 %, and 59.1 % respectively. Furthermore, for a given k_h value, when the value of φ is larger, the response of $N_{\gamma E}$ to η is more pronounced. For example, when $k_h = 0$, as the value of η increases from 5° to 30°, the value of $N_{\gamma E}$ corresponding to $\varphi = 30°$ decreases by 43.5 %, whereas for $\varphi = 40°$, the value of $N_{\gamma E}$ decreases by 59.6 %. From Fig. 11, as the value of η increases, the value of N_{cE} decreases linearly. However, the degree to which η affects N_{cE} varies depending on the value of k_h. Specifically, when the value of η increases from 5° to 40° and $\varphi = 30°$, with k_h values of 0.0, 0.1, 0.2, and 0.3, the value of N_{cE} decreases by 41.4 %, 38.3 %, 34.1 %, and 28.9 % respectively. Overall, the slope inclination has a significant impact on the seismic bearing capacity of a rectangular foundation.

5.2.3. *Effect of the distance to slope edge*

Assuming $\eta = 20°$, $l/b = 2$, Figs. 12 and 13 respectively show the variation of the seismic bearing capacity factors ($N_{\gamma E}$ and N_{cE}) with the distance to slope edge a/b, considering $k_h = 0.0$, 0.1, 0.2, 0.3 and $\varphi =$

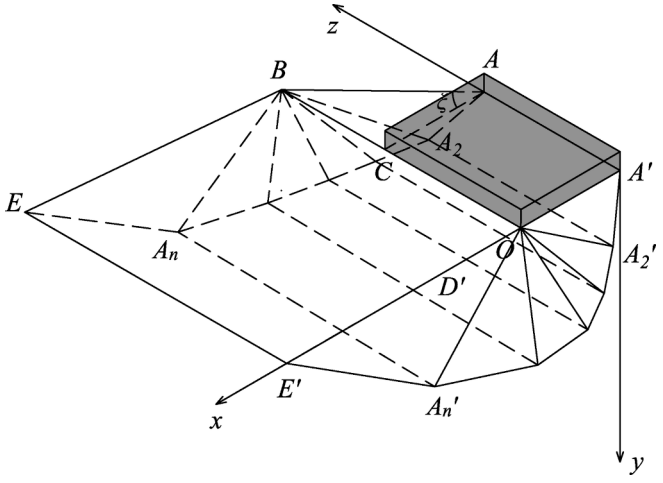

Fig. 14. The failure mechanism of a rectangular foundation when it is far enough from the slope.

Table 9
Seismic bearing capacity factor $N'_{\gamma E}$ of strip footings near slopes.

		$\eta = 10^\circ$				$\eta = 20^\circ$			
		a/b							
k_h	φ (°)	0	0.5	1	1.5	0	0.5	1	1.5
0.0	15	1.32	1.86	2.18	2.73	0.41	0.99	1.56	2.13
	20	3.06	3.93	4.57	5.28	1.48	2.56	3.60	4.62
	25	6.56	8.04	9.22	10.02	3.57	5.46	7.28	9.05
	30	13.94	16.50	18.67	20.45	7.81	11.10	14.28	17.28
	35	30.48	35.07	39.15	42.74	16.97	22.74	28.32	33.70
	40	70.75	79.46	87.46	94.82	38.01	48.68	58.98	69.03
	45	180.78	198.65	215.47	231.36	92.13	113.13	133.46	153.35
0.1	15	0.36	0.69	1.00	1.15	–	–	0.30	0.62
	20	1.46	2.08	2.57	2.74	0.41	1.06	1.68	2.30
	25	3.59	4.67	5.55	6.06	1.59	2.82	4.00	5.16
	30	8.13	10.00	11.59	12.88	4.06	6.28	8.41	10.50
	35	18.26	21.62	24.58	27.17	9.41	13.41	17.25	21.01
	40	42.63	48.93	54.69	59.95	21.73	29.13	36.26	43.23
	45	107.71	120.41	132.32	143.51	52.88	67.37	81.36	95.06
0.2	20	0.33	0.66	0.98	1.29	–	–	0.32	0.66
	25	1.55	2.27	2.89	3.23	0.39	1.11	1.79	2.46
	30	4.16	5.45	6.55	7.43	1.69	3.10	4.43	5.74
	35	10.02	12.36	14.43	16.21	4.49	7.25	9.75	12.21
	40	24.07	28.47	32.47	36.10	11.47	16.39	21.13	25.77
	45	61.03	69.80	77.99	85.65	28.62	38.30	47.63	56.77

30°, 40°. From Fig. 12, as the value of a/b increases, the value of $N_{\gamma E}$ initially increases linearly and then remains constant. The critical distance a/b, which corresponds to the inflection point of the change in $N_{\gamma E}$, varies with the value of φ and k_h. For example, when $\varphi = 30^\circ$, $k_h = 0.0$, this critical distance is $a/b = 2$; when $\varphi = 40^\circ$ $k_h = 0.0$, the critical distance is $a/b = 3.5$ For a giver value of φ, the critical distance will increase as k_h increases.

Fig. 13 shows that as the ratio a/b increases, N_{cE} initially increases linearly and then remains constant. Clearly, $N_{\gamma E}$ and N_{cE} respond to changes in a/b in essentially the same way. This indicates that when the rectangular foundation is beyond the critical distance from the slope, the influence of the slope on its bearing capacity can be neglected. At that time, the failure mechanism no longer extends to the slope surface, which is equivalent to failure mechanism occurring in a semi-infinite horizontal space, as shown in Fig. 14. It's worth mentioning that the critical distance for N_{cE} is different from that for $N_{\gamma E}$. For the same values of φ and k_h, the critical distance for N_{cE} is always greater than that for $N_{\gamma E}$. For example, when $\varphi = 30^\circ$, $k_h = 0.0$, the critical distance of N_{cE} is $a/b = 3.4$ while the critical distance of $N_{\gamma E}$ is $a/b = 2.0$.

Table 10
Seismic bearing capacity factor N'_{cE}.of strip footings near slopes.

		$\eta = 10^\circ$				$\eta = 20^\circ$			
		a/b							
k_h	φ (°)	0	0.5	1	1.5	0	0.5	1	1.5
0.0	15	9.70	10.02	10.32	10.60	8.49	9.07	9.59	10.06
	20	12.80	13.20	13.58	13.94	10.92	11.65	12.30	12.91
	25	17.39	17.90	18.40	18.87	14.43	15.34	16.17	16.95
	30	24.51	25.18	25.82	26.44	19.67	20.83	21.91	22.92
	35	36.17	37.06	37.92	38.75	27.93	29.44	30.85	32.19
	40	56.64	57.86	59.03	60.18	41.77	43.79	45.70	47.51
	45	95.90	97.62	99.31	100.95	66.93	69.72	72.38	75.30
0.1	15	8.38	8.71	9.02	9.31	7.34	7.94	8.46	8.93
	20	10.92	11.34	11.72	12.08	9.34	10.07	10.72	11.31
	25	14.64	15.16	15.64	16.11	12.16	13.06	13.88	14.64
	30	20.31	20.97	21.59	22.19	16.32	17.45	18.49	19.45
	35	29.42	30.27	31.09	31.88	22.74	24.18	25.52	26.78
	40	45.04	46.18	47.29	48.36	33.26	35.14	36.92	38.60
	45	74.19	75.77	77.32	78.82	51.85	54.41	56.83	59.15
0.2	15	7.04	7.39	7.70	7.99	6.27	6.80	7.32	7.79
	20	9.09	9.51	9.89	10.25	7.80	8.52	9.16	9.74
	25	12.04	12.55	13.03	13.48	10.03	10.91	11.70	12.43
	30	16.46	17.10	17.70	18.28	13.26	14.35	15.34	16.25
	35	23.44	24.25	25.02	25.77	18.15	19.52	20.77	21.95
	40	35.13	36.20	37.22	38.21	25.99	27.75	29.38	30.92
	45	56.38	57.83	59.23	60.59	39.47	41.80	44.00	46.08

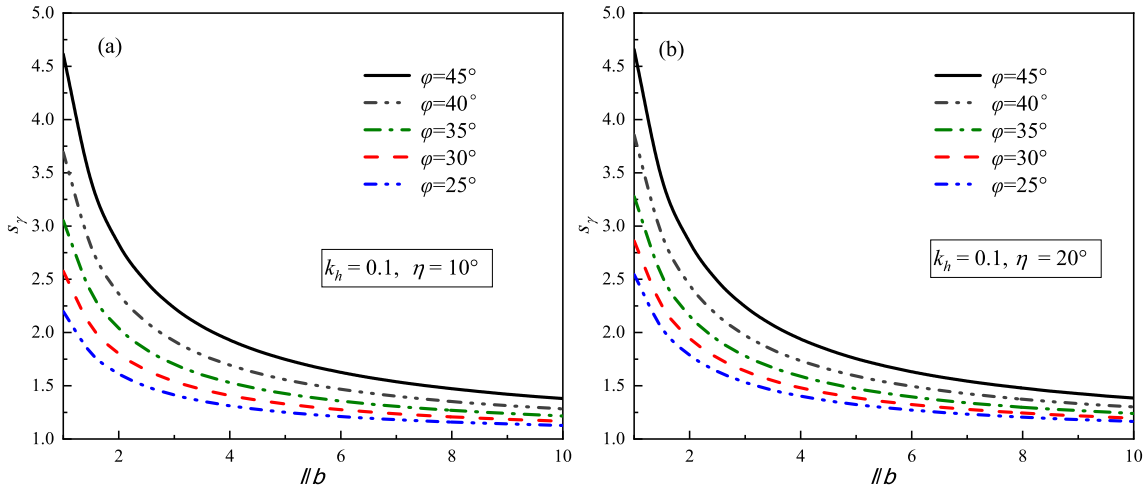

Fig. 15. The variation of s_γ with l/b for different values of φ considering (a) $\eta = 10°$ and (b) $\eta = 20°$ ($k_h = 0.1$).

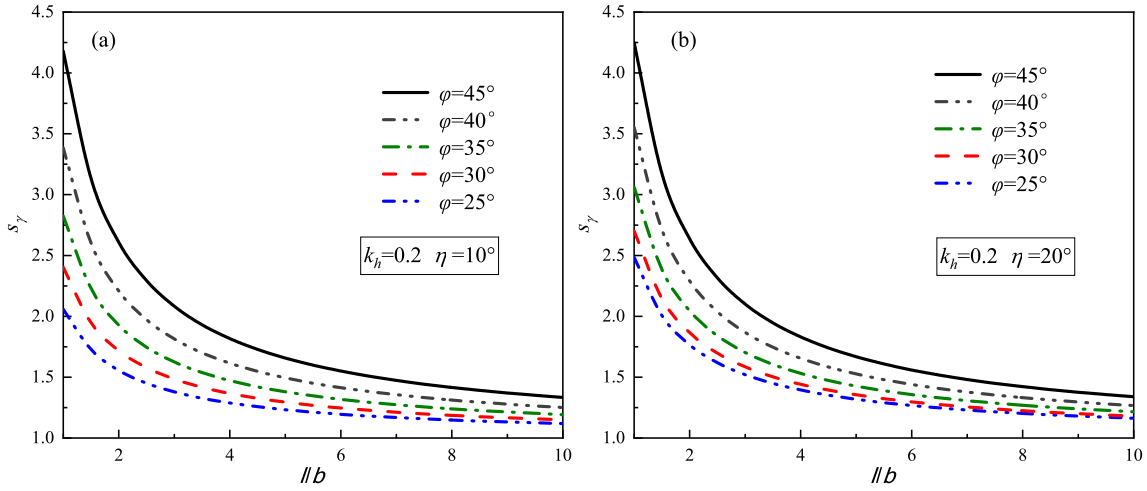

Fig. 16. The variation of s_γ with l/b for different values of φ considering (a) $\eta = 10°$ and (b) $\eta = 20°$ ($k_h = 0.2$).

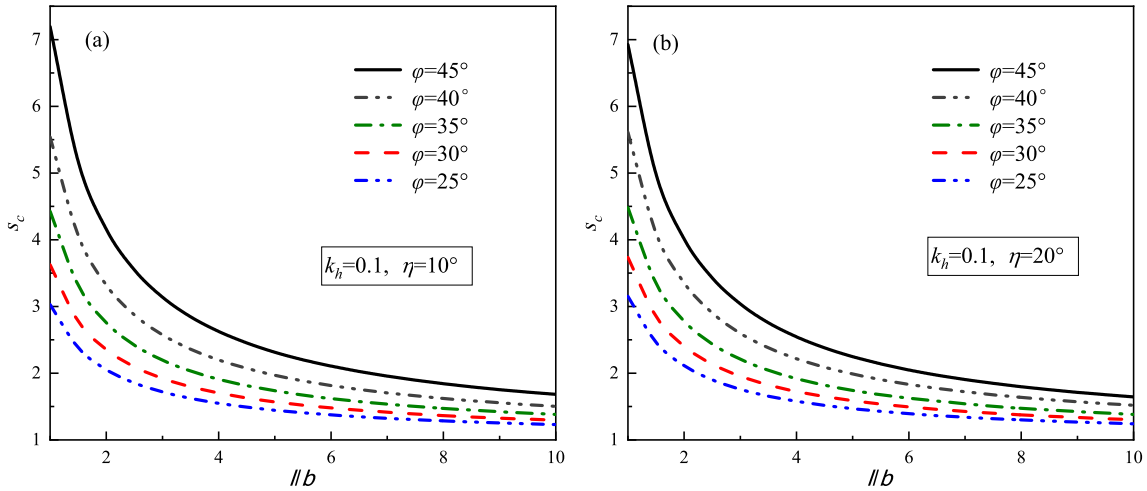

Fig. 17. The variation of s_c with l/b for different values of φ considering (a) $\eta = 10°$ and (b) $\eta = 20°$ ($k_h = 0.1$).

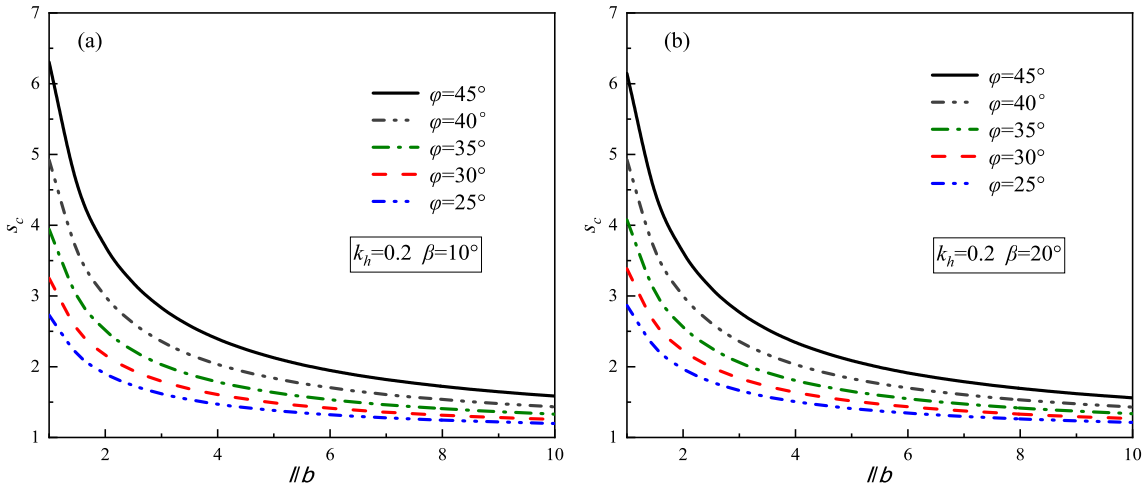

Fig. 18. The variation of s_c with l/b for different values of φ considering (a) $\eta = 10^\circ$ and (b) $\eta = 20^\circ$ ($k_h = 0.2$).

5.3. Shape factor

A dimensionless shape factor has been introduced to quantify the size-related impact on q_u. This factor is calculated by taking the ratio of the seismic bearing capacity of a rectangular foundation near a slope to that of a strip footing in the same proximity to the slope. The detailed expression is presented below:

$$s_\gamma = \frac{N_{\gamma E}}{N'_{\gamma E}} \tag{17}$$

$$s_c = \frac{N_{cE}}{N'_{cE}} \tag{18}$$

where s_γ and s_c respectively represent shape factors related to γ and c. $N'_{\gamma E}$ and N'_{cE} are seismic bearing capacity factors for strip footings adjacent to a slope. Tables 9 and 10 respectively record the values of $N'_{\gamma E}$ and N'_{cE} for different parameter combinations, which are calculated based on the multi-block failure mechanism shown in Fig. 3. The specific calculation process can be referred to Askari and Farzaneh (2003).

The design charts of the obtained shape factor with aspect ratio l/b for different values of φ are shown in Figs. 15-18 ($\eta = 10^\circ$, 20° and $k_h = 0.1$, 0.2). Figs. 15 and 16 illustrate the variation of s_γ while Figs. 17 and 18 show the variation of s_c. It can be observed that, for all different values of φ, as the value of l/b increases, the s_γ and s_c values keep decreasing. Moreover, the rate of decrease also gradually slows down. Ultimately, the s_γ and s_c values all converges to 1. This trend is consistent with that reflected in Figs. 8 and 9 When other calculation parameters are constant, the values of s_γ and s_c increase with the increase of φ. For instance, when $l/b = 1$, $\eta = 10^\circ$, $k_h = 0.1$, as φ increases from 25° to 45°, the values of s_γ and s_c increase by 2.42 and 4.17 respectively. This is because the seismic bearing capacity of the rectangular foundation is more sensitive to changes in the internal friction angle. Additionally, as the value of k_h increases, the values of s_γ and s_c decrease slightly. For example, when $l/b = 1$, $\eta = 10^\circ$, $\varphi = 25^\circ$, the s_γ values corresponding to $k_h = 0.1$ and $k_h = 0.2$ are 2.20 and 2.06 respectively; while the s_c values are 3.03 and 2.73 respectively. This reflects the more significant impact of seismic loads on the bearing capacity of rectangular foundations. From an engineering perspective, these design charts can be easily used to obtain shape factors under different working conditions. According to Eqs. (17) and (18), by multiplying the shape factors by the seismic bearing capacity factor of a strip footing, the seismic bearing capacity factor of a rectangular strip foundation can be calculated.

5.4. Critical 3D failure mechanism

Assuming $a/b = 1$, $l/b = 2$, $\eta = 20^\circ$, Figs. 19 and 20 show the variation of front view and side view of 3D failure mechanisms for different values of k_h ($k_h = 0.0$, 0.1, and 0.2) and different values of φ ($\varphi = 20^\circ$, 30°, and 40°) respectively. The contours of the failure surfaces are represented by blue lines. As shown in Fig. 19, with the increase of k_h, the 3D failure mechanism decreases in size in the x, y, and z directions. Under increasingly intense seismic loads, the geometry of the 3D failure mechanism gradually shifts laterally from the depth direction, becoming progressively flatter. Additionally, as the distance to the slope surface decreases, the span of the failure zone in the z-direction almost increases linearly (from line AA' to EE'). It is also notable that the area of the bottom of the 3D failure mechanism is smaller than that of the top, indicating that the side surfaces are inclined. From Fig. 20, it can be observed that with an increase in φ, the overall size of the 3D failure mechanism significantly expands. Specifically, for every 10° increase in φ, the maximum extension distance of the sliding surface at the bottom of the failure mechanism in the x, y, and z directions expands by approximately 1.3 times. For example, when $\varphi = 20^\circ$, the maximum extension distances of the sliding surface at the bottom of the failure mechanism in the x, y, and z directions are 2.74 m, 0.75 m, and 1.59 m, respectively. However, when $\varphi = 30^\circ$, these distances increase to 3.61 m, 1.01 m, and 2.01 m, respectively.

6. Conclusions

Using the upper bound method, this paper provides, for the first time, explicit expressions for calculating the seismic bearing capacity of rectangular foundations near slopes. Initially, a 3D failure mechanism based on Michalowski (1989) and the corresponding velocity field are established. Each sliding surface of this 3D failure mechanism follows the associated flow rule. Subsequently, the power of all external forces and the dissipation of internal energy are calculated, where the seismic loads are simulated using the pseudo-static method. Finally, by solving the energy balance equation and employing the SQP optimization algorithm, the minimum seismic bearing capacity can be obtained. To fully validate the accuracy of the proposed theoretical framework, the results of this paper are compared in detail with the results from other literature and numerical simulation results. In addition, the influence of various parameters, the shape factor, and the critical failure mechanisms are all thoroughly investigated. The main conclusions can be listed as:

(1) A simplified method for calculating the seismic bearing capacity q_u has been provided: the superposition method. This method

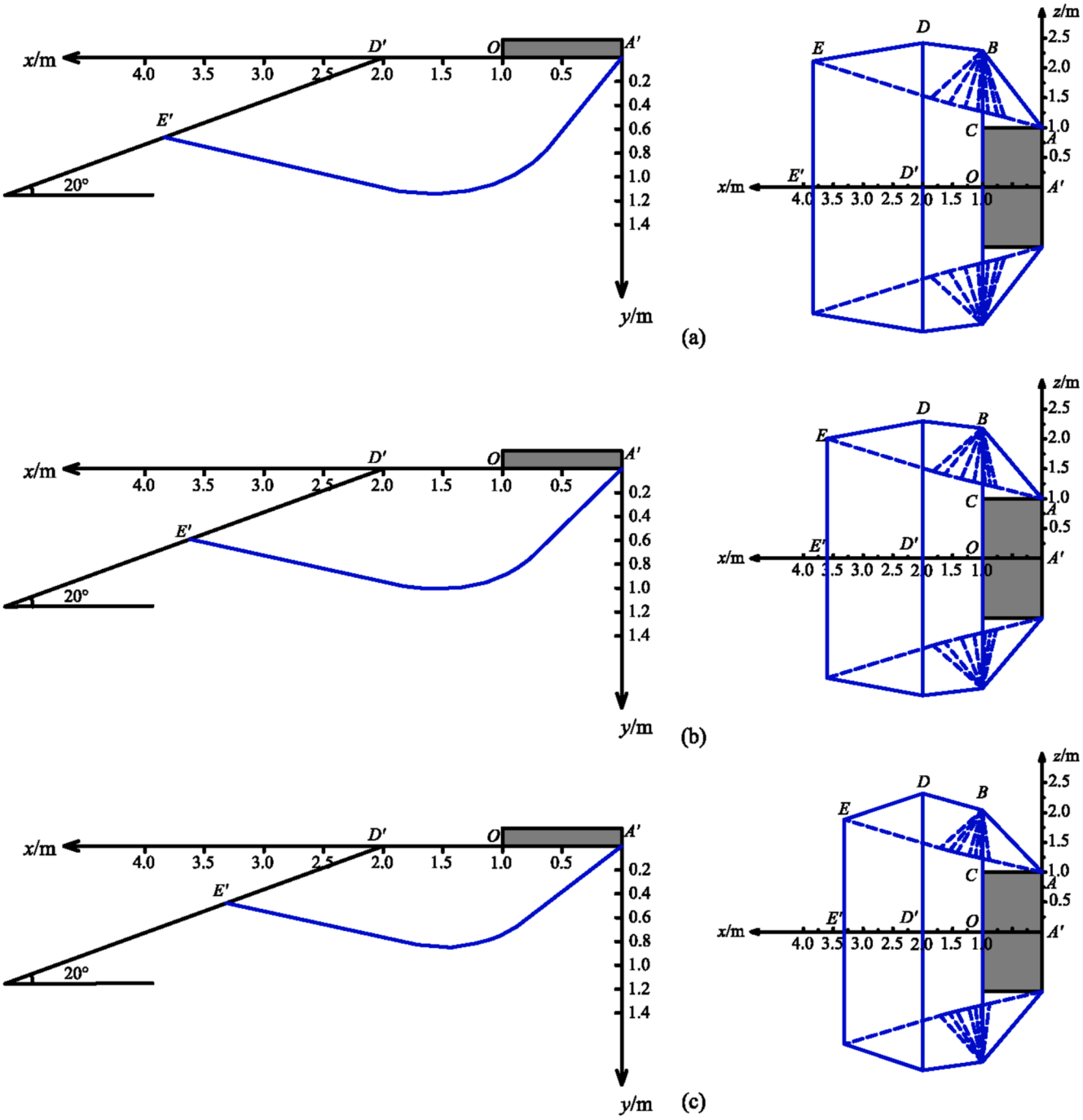

Fig. 19. Front view and side view of 3D failure mechanisms for (a) $k_h = 0.0$, (b) $k_h = 0.1$, and (c) $k_h = 0.2$ ($a/b = 1$, $l/b = 2$, $\eta = 20°$, $\varphi = 30°$).

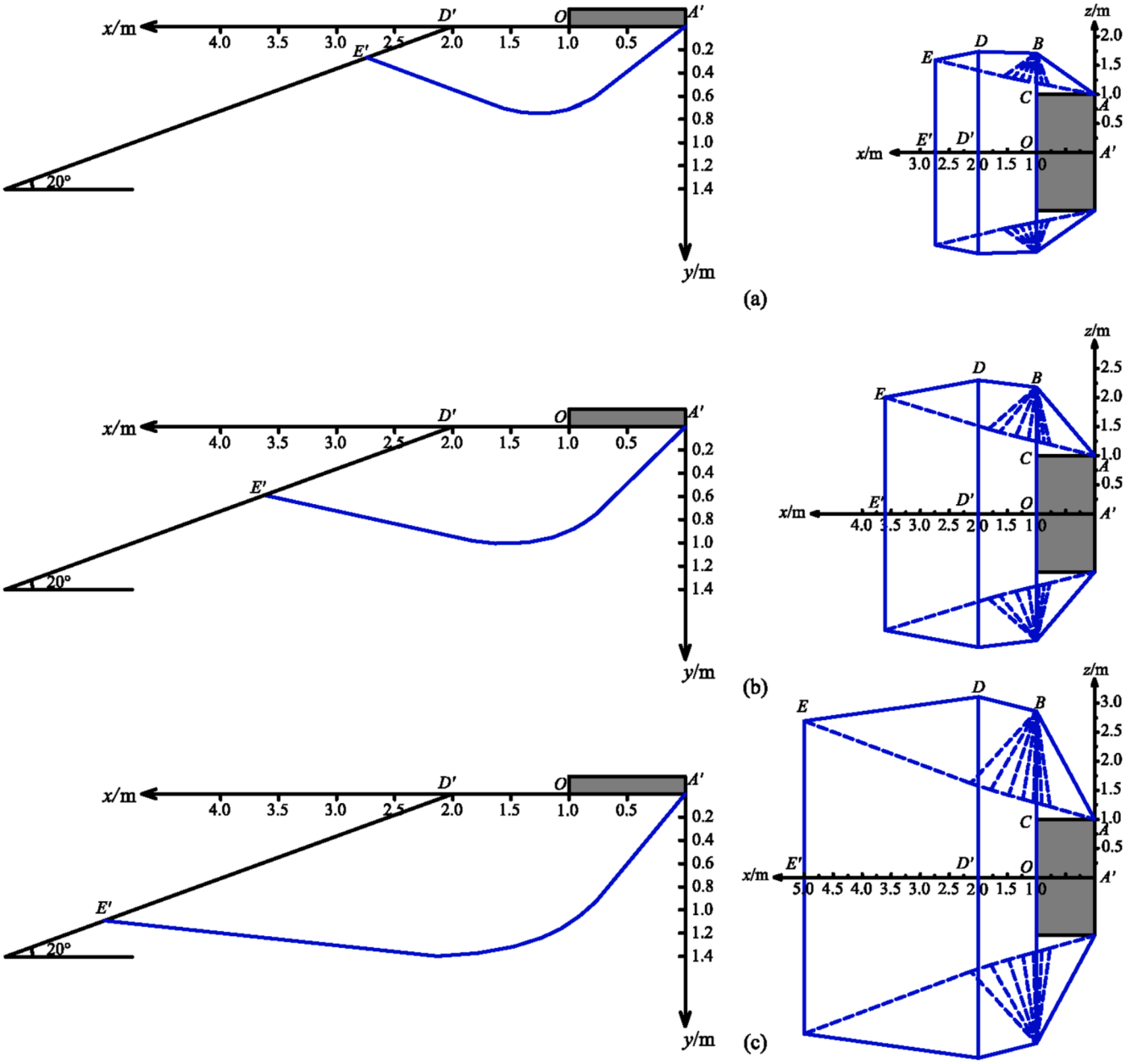

Fig. 20. Front view and side view of 3D failure mechanisms for (a) $\varphi = 20^\circ$, (b) $\varphi = 30^\circ$, and (c) $\varphi = 40^\circ$ ($a/b = 1$, $l/b = 2$, $\eta = 20^\circ$, $k_h = 0.1$).

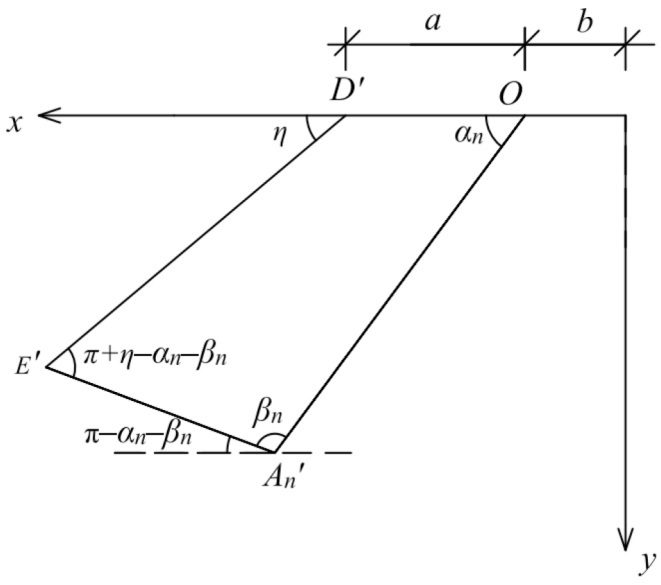

Fig. 21. Section view of the *n*th block along *xoy* plane.

involves separately calculating the magnitudes of different bearing capacity components and then obtaining the results based on Terzaghi's equation. Although its solution is not a strictly upper bound solution, it is acceptable in design. This method is applicable to both cohesive and frictional soils. The seismic bearing capacity factors $N_{\gamma E}$ and N_{cE} under different conditions are recorded in Tables 7 and 8, respectively.

(2) Parametric analysis shows that as the value of l/b increases, the values of $N_{\gamma E}$ and N_{cE} continuously decrease, but the rate of decrease slows down. This indicates that they will eventually converge to a fixed value. With an increase of slope inclination, the values of $N_{\gamma E}$ and N_{cE} decrease linearly, and the reduction is more pronounced with a larger value of φ. As the distance of the rectangular foundation from the slope edge a increases, the value of $N_{\gamma E}$ and N_{cE} first increases linearly and then remains constant, indicating that the failure of rectangular foundation gradually transitions to occurring in a horizontally infinite space.

(3) Analysis of the shape factor reveals that an increase in the aspect ratio reduces the shape factor, but the rate of reduction diminishes. With an increase in φ and k_h values, the shape factor decreases, as the seismic bearing capacity of the rectangular foundation is more sensitive to changes in the φ and k_h values.

(4) Analysis of the critical failure mechanism shows that the bottom area of the 3D failure mechanism is smaller than the top area. An increase in the value of k_h reduces the overall size of the failure mechanism, making it flatter, while increasing φ value causes the failure mechanism to expand sharply in all directions.

(5) The analysis provided can be improved by including the 3D failure mechanism below the slope toe and considering the foundation-soil interface roughness.

CRediT authorship contribution statement

Sheng Xu: Writing – original draft, Software, Investigation. **Xiao-Li Yang:** Methodology. **Zhen-Yu Yin:** Writing – review & editing, Validation.

Declaration of competing interest

The authors declare that they have no known competing financial interests or personal relationships that could have appeared to influence the work reported in this paper.

Acknowledgment

This research was supported by the European Union (EU) - Hong Kong Research and Innovation Cooperation Co-funding Mechanism by the Research Grants Council of Hong Kong (RGC) (Grant No.: E-PolyU501/24) and the Research Centre for Nature-based Urban Infrastructure Solutions at The Hong Kong Polytechnic University.

Appendix A

According to the associated flow rule, the end surfaces of the 3D failure mechanism are constructed in the following steps:

The coordinates (x and y) of points $(A,A_2,\cdots,A_{n-1},A_n,E)$ on the end surface are equal to the coordinates of the corresponding points $(A',A_2',\cdots,A_{n-1}',A_n',E')$ on the xoy plane, as shown in Fig. 4. According to the sine theorem,

$$\left|OA_i'\right| = b\prod_{j=1}^{i-1}\frac{\sin\beta_j}{\sin(\alpha_j+\beta_j)}\ 2\leqslant i\leqslant n-1 \tag{19}$$

where $\left|OA_i'\right|$ represents the length of the line segment OA_i'. Therefore, the x and y coordinates of the end surface points $(A',A_2',\cdots,A_{n-1}',A_n',E')$ are:

$$x_i = b-\left|OA_i'\right|\cos(\sum_{j=1}^{i-1}\alpha_j) \tag{20}$$

$$y_i = \left|OA_i'\right|\sin(\sum_{j=1}^{i-1}\alpha_j) \tag{21}$$

For the n-th block, its profile is shown in Fig. 21. In the x direction,

$$a+\left|D'E'\right|\cos\eta = \left|OA_n'\right|\cos\alpha_n+\left|A_n'E'\right|\cos(\pi-\alpha_n-\beta_n) \tag{22}$$

where $\left|D'E'\right|$, $\left|OA_n'\right|$, $\left|A_n'E'\right|$ represents the length of the line segment $D'E'$, OA_n', $A_n'E'$ respectively. In the y direction,

$$\left|D'E'\right|\cos\eta+\left|A_n'E'\right|\sin(\pi-\alpha_n-\beta_n) = \left|OA_n'\right|\sin\alpha_n \tag{23}$$

By combining Eqs. (22) and (23) and solving them, we can get:

$$\left|A_n'E'\right| = \frac{\left|OA_n'\right|\sin(\alpha_n - \eta) + a\sin\eta}{\sin(\alpha_n + \beta_n - \eta)} \tag{24}$$

Hence, the x and y coordinates of ponit E' are:

$$x_{E'} = b + \left|OA_n'\right|\cos\alpha_n - \left|A_n'E'\right|\cos(\alpha_n + \beta_n) \tag{25}$$

$$y_{E'} = \left|OA_n'\right|\sin\alpha_n - \left|A_n'E'\right|\sin(\alpha_n + \beta_n) \tag{26}$$

Consequently, for the sliding surface ABA_2, the sole unknown coordinate among the three vertices is the z-coordinate of point A_2. The spatial equation of the sliding surface ABA_2, derived from the cross product operation of vectors, is formulated as follows:

$$Ax + By + Cz + D = 0 \tag{27}$$

$\overrightarrow{n} = (A, B, C)$ is he normal vector of the plane ABA_2, which can be obtained from the fork multiplication of vector $\overrightarrow{BA}$ with vector $\overrightarrow{BA_2}$. $\overrightarrow{v_i} = (\cos(\beta_i - \sum_{j=1}^{i-1}\alpha_j - \varphi), \sin(\beta_i - \sum_{j=1}^{i-1}\alpha_j - \varphi), 0)$ is the unit vector of the i-th block velocity vector. According to the associated flow rule, the sliding surface of each block is at an angle of φ with the velocity vector. Therefore, for the end surface, ABA_2,the following equation can be derived:

$$\frac{A\cos(\beta_1 - \varphi) + B\sin(\beta_1 - \varphi)}{\sqrt{A^2 + B^2 + C^2}} = \sin\varphi \tag{28}$$

By solving Eq. (28), the z-coordinate of A_2 is determined. For the subsequent sliding surface, the same method can be applied to solve for the z-coordinate of A_3. In this way, after n iterations of point-to-point solving, the coordinates of all points on the end surface $BAA_2A_3\cdots A_nED$ are obtained.

All blocks in the 3D failure mechanism can be decomposed into tetrahedra. Assuming the coordinates of the tetrahedron's vertices are (x_i,y_i,z_i) $(i = 1,2,3,4)$, the volume of the tetrahedron can be calculated using the following formula:

$$V = \frac{1}{6}\begin{vmatrix} x_1 & y_1 & z_1 & 1 \\ x_2 & y_2 & z_2 & 1 \\ x_3 & y_3 & z_3 & 1 \\ x_4 & y_4 & z_4 & 1 \end{vmatrix} \tag{29}$$

All sliding surfaces of the 3D failure mechanism are either triangular or quadrilateral. Quadrilaterals can be divided into two triangles for area calculation. Assuming the vertex coordinates of a triangle are (x_i, y_i, z_i) $(i = 1,2,3)$, the area calculation formula for the triangle is given by:

$$S = \frac{1}{2}\sqrt{\begin{vmatrix} y_2 - y_1 & z_2 - z_1 \\ y_3 - y_1 & z_3 - z_1 \end{vmatrix}^2 + \begin{vmatrix} z_2 - z_1 & x_2 - x_1 \\ z_3 - z_1 & x_3 - x_1 \end{vmatrix}^2 + \begin{vmatrix} x_2 - x_1 & y_2 - y_1 \\ x_3 - x_1 & y_3 - y_1 \end{vmatrix}^2} \tag{30}$$

Data availability

Data will be made available on request.

References

Antao, A., da Silva, M.V., Guerra, N., Delgado, R., 2012. An upper bound-based solution for the shape factors of bearing capacity of footings under drained conditions using a parallelized mixed fe formulation with quadratic velocity fields. Comput Geotech. 41, 23–35. https://doi.org/10.1016/j.compgeo.2011.11.003.

Askari, F., Farzaneh, O., 2003. Upper-bound solution for seismic bearing capacity of shallow foundations near slopes. Geotechnique. 53 (8), 697–702. https://doi.org/10.1680/geot.53.8.697.37400.

Cao, W.-G., Yuan, Q.-S., Hu, W.-D., 2016. Upper bound solution for ultimate bearing capacity of the shallow rectangular footings adjacent to slope. Journal of Hunan University Natural Sciences. 43 (11).

Castelli, F., Motta, E., 2010. Bearing capacity of strip footings near slopes. Geotech Geol Eng. 28, 187–198. https://doi.org/10.1007/s10706-009-9277-9.

Chen, W.F., 1975. Limit analysis and soil plasticity. Elsevier.

Chwała, M., 2019. Undrained bearing capacity of spatially random soil for rectangular footings. Soils Found. 59 (5), 1508–1521. https://doi.org/10.1016/j.sandf.2019.07.005.

De Buhan, P., Garnier, D., 1998. Three dimensional bearing capacity analysis of a foundation near a slope. Soils Found. 38 (3), 153–163. https://doi.org/10.3208/sandf.38.3_153.

Ganjian, N., Askari, F., Farzaneh, O., 2009. Bearing capacity of rectangular foundations near the slopes with nonassociated flow rules. Proc Inst Civ Eng-Fo 265–277. https://doi.org/10.1061/41082(362)27.

Gourvenec, S., 2007. Shape effects on the capacity of rectangular footings under general loading. Géotechnique. 57 (8), 637–646. https://doi.org/10.1680/geot.2007.57.8.637.

Hou, C., Yang, X., 2022. 3d stability analysis of tunnel face with influence of unsaturated transient flow. Tunn Undergr Sp Tech. 123, 104414. https://doi.org/10.1016/j.tust.2022.104414.

Izadi, A., Foroutan Kalourazi, A., Jamshidi Chenari, R., 2021a. Effect of roughness on seismic bearing capacity of shallow foundations near slopes using the lower bound finite element method. Int J Geomech. 21 (3), 06020043. https://doi.org/10.1061/(ASCE)GM.1943-5622.0001935.

Izadi, A., Jamshidi Chenari, R., Javankhshdel, S., Hemmati Masouleh, F., 2022. Effect of love wave propagation on the equivalent seismic bearing capacity of shallow foundations using 3d coulomb failure mechanism. Geotech Geol Eng. 40 (5), 2781–2797. https://doi.org/10.1007/s10706-022-02061-5.

Izadi, A., Nazemi Sabet Soumehsaraei, M., Jamshidi Chenari, R., Moallemi, S., Javankhoshdel, S., 2021b. Spectral bearing capacity analysis of strip footings under pseudo-dynamic excitation. Geomech Geoengin. 16 (5), 359–378. https://doi.org/10.1080/17486025.2019.1670873.

Kalourazi, A.F., Izadi, A., Chenari, R.J., 2019. Seismic bearing capacity of shallow strip foundations in the vicinity of slopes using the lower bound finite element method. Soils Found. 59 (6), 1891–1905. https://doi.org/10.1016/j.sandf.2019.08.014.

Kawa, M., Puła, W., Suska, M., 2016. Random analysis of bearing capacity of square footing using the las procedure. Stud Geotech Mech. 38 (3), 3–13. https://doi.org/10.1515/sgem-2016-0021.

Krabbenhoft, K., Lyamin, A.V., Hjiaj, M., Sloan, S.W., 2005. A new discontinuous upper bound limit analysis formulation. Int J Numer Meth Eng. 63 (7), 1069–1088. https://doi.org/10.1002/nme.1314.

Kumar, J., Ghosh, P., 2006. Seismic bearing capacity for embedded footings on sloping ground. Geotechnique. 56 (2), 133–140. https://doi.org/10.1680/geot.2006.56.2.133.

Li, S., Yu, J., Huang, M., Leung, C., 2021. Upper bound analysis of rectangular surface footings on clay with linearly increasing strength. Comput Geotech. 129, 103896. https://doi.org/10.1016/j.compgeo.2020.103896.

Li, Z.-W., Yang, X.-L., Li, T.-Z., 2020. Static and seismic stability assessment of 3d slopes with cracks. Eng Geol. 265, 105450. https://doi.org/10.1016/j.enggeo.2019.105450.

Lyamin, A., Salgado, R., Sloan, S., Prezzi, M., 2007. Two-and three-dimensional bearing capacity of footings in sand. Géotechnique. 57 (8), 647–662. https://doi.org/10.1680/geot.2007.57.8.647.

Maghferati, S.P., Chenari, R.J., Lajevardi, S.H., Payan, M., Mirhosseini, S.M., 2023. Seismic combined bearing capacity of strip footings on partially saturated soils using lower bound theorem of finite element limit analysis and second-order cone programming. Comput Geotech. 157, 105327. https://doi.org/10.1016/j.compgeo.2023.105327.

Mansouri, M., Imani, M., Fahimifar, A., 2019. Ultimate bearing capacity of rock masses under square and rectangular footings. Comput Geotech. 111, 1–9. https://doi.org/10.1016/j.compgeo.2019.03.002.

Michalowski, R., 1989. Three-dimensional analysis of locally loaded slopes. Geotechnique. 39 (1), 27–38. https://doi.org/10.1016/0148-9062(89)91254-0.

Michalowski, R., 1997. An estimate of the influence of soil weight on bearing capacity using limit analysis. Soils Found. 37 (4), 57–64. https://doi.org/10.3208/sandf.37.4_57.

Michalowski, R., 2001. Upper-bound load estimates on square and rectangular footings. Géotechnique. 51 (9), 787–798. https://doi.org/10.1002/nme.1314.

Mohapatra, D., Kumar, J., 2019. Collapse loads for rectangular foundations by three-dimensional upper bound limit analysis using radial point interpolation method. Int J Numer Anal Met. 43 (2), 641–660. https://doi.org/10.1002/nag.2885.

Osman, A.S., 2019. Upper bound solutions for the shape factors of smooth rectangular footings on frictional materials. Comput Geotech. 115, 103177. https://doi.org/10.1016/j.compgeo.2019.103177.

Safardoost Siahmazgi, A., Fathipour, H., Jamshidi Chenari, R., Veiskarami, M., Payan, M., 2022. Evaluation of the pseudo-dynamic bearing capacity of surface footings on cohesionless soils using finite element lower bound limit analysis. Geomech Geoengin. 17 (3), 765–777. https://doi.org/10.1080/17486025.2021.1889686.

Salgado, R., Lyamin, A., Sloan, S., Yu, H., 2004. Two-and three-dimensional bearing capacity of foundations in clay. Géotechnique. 54 (5), 297–306. https://doi.org/10.1680/geot.2004.54.5.297.

Sloan, S., 1989. Upper bound limit analysis using finite elements and linear programming. Int J Numer Anal Met. 13 (3), 263–282. https://doi.org/10.1002/nag.1610130304.

Soubra, A.-H., 1999. Upper-bound solutions for bearing capacity of foundations. J Geotech Geoenviron. 125 (1), 59–68. https://doi.org/10.1061/(ASCE)1090-0241(1999)125:1(59).

Soufi, G.R., Chenari, R.J., Javankhoshdel, S., 2021. Conventional vs. Modified pseudo-dynamic seismic analyses in the shallow strip footing bearing capacity problem. Earthq Eng Eng Vib. 20, 993–1006. https://doi.org/10.1007/s10706-022-02061-5.

Tavakoli, M.A., Fathipour, H., Payan, M., Chenari, R.J., Ahmadi, H., 2023. Seismic bearing capacity of shallow foundations subjected to inclined and eccentric loading using modified pseudo-dynamic method. Transp Geotech. 40, 100979. https://doi.org/10.1016/j.trgeo.2023.100979.

Wang, H., Yang, M., 2005. Approximate upper-bound solution for bearing capacity of rectangular footings near excavations. Chinese Journal of Geotechnical Engineering. 27 (10), 1116–1122.

Xu, S., Liu, J., Yang, X.-L., 2023. Pseudo-dynamic analysis of a 3d tunnel face in inclined weak strata. Undergr Space. 12, 156–166. https://doi.org/10.1016/j.undsp.2023.03.002.

Yamamoto, K., 2010. Seismic bearing capacity of shallow foundations near slopes using the upper-bound method. Int J Geotech Eng. 4 (2), 255–267. https://doi.org/10.3328/ijge.2010.04.02.255-267.

Yang, H., Shen, Z., Wang, J., 2003. 3d lower bound bearing capacity of smooth rectangular surface footings. Mech Res Commun. 30 (5), 481–492. https://doi.org/10.1016/s0093-6413(03)00047-8.

Yang, X.-L., 2009. Seismic bearing capacity of a strip footing on rock slopes. Can Geotech J. 46 (8), 943–954. https://doi.org/10.1139/t09-038.

Zhang, Z., Yang, X., 2023. Unified solution of safety factors for three-dimensional compound slopes considering local and global instability. Comput Geotech. 155, 105227. https://doi.org/10.1016/j.compgeo.2022.105227.

Zhong, J.-H., Yang, X.-L., 2022. Pseudo-dynamic stability of rock slope considering hoek–brown strength criterion. Acta Geotech. 17 (6), 2481–2494. https://doi.org/10.1007/s11440-021-01425-0.

Zhu, D., 2000. The least upper-bound solutions for bearing capacity factor Nγ. Soils Found. 40 (1), 123–129. https://doi.org/10.3208/sandf.40.123.